Analytic characterization of random errors in spectral dual-polarized cloud radar observations

Alexander Myagkov[1] and Davide Ori[2]

[1]Radiometer Physics GmbH, Meckenheim, Germany
[2]Institute for Geophysics and Meteorology, University of Cologne, Cologne, Germany

Correspondence: Alexander Myagkov (alexander.myagkov@radiometer-physics.de)

Abstract. This study presents the first-ever complete characterization of random errors in dual-polarimetric spectral observations of meteorological targets by cloud radars. The characterization is given by means of mathematical equations for joint probability density functions (PDF) and error covariance matrices. The derived equations are checked for consistency using real radar measurements. One of the main conclusions of the study is that the convenient representation of spectral polarimetric measurements including differential reflectivity Z_{DR}, correlation coefficient ρ_{HV}, and differential phase Φ_{DP} is not suited for the proper characterization of the error covariance matrix. This is because the aforementioned quantities are complex, non-linear functions of the radar raw data and thus their error covariance matrix is commonly derived using simplified linear relations and by neglecting the correlation of errors. This study formulates the spectral polarimetric measurements in terms of a different set of quantities that allows for a proper analytic treatment of their error covariance matrix. The results given in this study allow for utilization of spectral polarimetric measurements for advanced meteorological applications, among which are variational retrieval techniques, data assimilation, and sensitivity analysis.

1 Introduction

Cloud radars are a major component of state-of-the-art, ground-based observation platforms (Illingworth et al., 2007; Kollias et al., 2020). Their unique capabilities make these instruments extremely valuable for cloud and precipitation research. First, these radars have Doppler capabilities, i.e. can independently characterize hydrometeors coexisting in the same volume but moving with different speeds relative to the radar (Kollias et al., 2007). Second, the high sensitivity and vast dynamic range make cloud radars capable of measuring return signals from a wide range of particles sizes, which is a challanging task for other instruments like lidars (Bühl et al., 2013). Third, due to relatively low attenuation of microwave signals by liquid water, cloud radars profile clouds up to the top even in presence of light-to-moderate rain. These capabilities promote cloud radars for investigation of different formation and development processes throughout the lifecycle of clouds. For instance, cloud radars help to characterize initial ice formation and development in mixed-phase clouds (Bühl et al., 2019), improve characterization of pure liquid clouds (Rusli et al., 2017; Acquistapace et al., 2017), estimate rates of aggregation (Kneifel et al., 2015, 2016) and riming (Kalesse et al., 2015; Moisseev et al., 2017; Kneifel and Moisseev, 2020), and quantitatively analyse solid and liquid precipitation (Matrosov, 2005; Matrosov et al., 2006, 2008; Tridon and Battaglia, 2015; Tridon et al., 2017, 2019).

Many cloud radars have dual-polarization capabilities. An interest in polarimetry-based methods in the cloud radar community has been growing, which is indicated by a number of studies during the last decade (Matrosov et al., 2012; Oue et al., 2015; Lu et al., 2015; Myagkov et al., 2016a, b; Matrosov et al., 2017; Oue et al., 2018; Myagkov et al., 2020). Vertically pointed cloud radars often operate in the LDR-mode (Linear Depolarization Ratio), i.e transmit a linearly-polarized wave (either horizontally or vertically) and receive co- and cross-polarized components of the backscattered signal (e.g Görsdorf et al., 2015). The LDR-mode is efficient for clutter removing and detection of the melting layer and columnar-shaped ice particles. As shown by Matrosov et al. (2001), however, the applicability of the LDR mode at low elevation angles might be limited due to its high sensitivity to the orientation of cloud particles. Therefore, scanning polarimetric cloud radars often have polarimetric modes which are less sensitive to the orientation. One of such modes is the hybrid mode (also denoted as the STSR (Simultaneous Transmittion and Simultaneous Reception) or STAR (Simulteneous Transmittion And Reception) mode in literature). Radars with the hybrid mode emit the horizontal and vertical components of the transmitted wave simultaneously (Myagkov et al., 2015; Bringi and Chandrasekar, 2001, Sec. 4.7). Cloud radars with the hybrid mode allow for adoption of polarimetry-based methods having been developed during last several decades for centimetre-wavelength meteorological radars (further denoted as precipitation radars).

Operational precipitation radars are used by weather services to continuously scan the atmosphere providing polarimetric variables integrated for a scattering volume. In addition to the integrated quantities, cloud radars with the hybrid mode enable spectrally-resolved polarimetric observations and, therefore, can provide the same set of polarimetric variables for different types of cloud particles coexisting in the same resolution volume (Oue et al., 2015; Myagkov et al., 2016b, 2020). Spectral observations are in general possible with precipitation radars (Spek et al., 2008; Dufournet and Russchenberg, 2011; Pfitzenmaier et al., 2018). Such measurements, however, are not performed by operational radars due to fast azimuth scanning.

Spectral polarimetry can be used for a development of advanced retrieval methods. For example variational retrievals developed for dual-frequency spectra (Tridon and Battaglia, 2015; Tridon et al., 2017) could be applied also to spectral polarimetry. Moisseev and Chandrasekar (2007) presented first attempts to retrieve profiles of raindrop-size distributions using polarimetric spectra from a precipitation radar. This approach, however, has not been yet explored in polarimetric cloud radars.

Recent review studies (Zhang et al., 2019; Morrison et al., 2020; Ryzhkov et al., 2020) demonstrate that polarimetric observations from precipitation radar networks are highly beneficial for the evaluation and development of numerical weather prediction and cloud resolving models. The high value of polarimetric observations is given by their sensitivity to microphysical properties of cloud and precipitation particles such as size, shape, number concentration, state of matter, density, and orientation (Kumjian, 2013). Polarimetric cloud radars are not yet widely used for model improvement. This, however, does not indicate that cloud radar polarimetry is not informative relative to precipitation radars. Conversely, the cloud radar spectral polarimetry can essentially complement available measurements.

The development of both quantitative retrievals and data assimilation algorithms requires the characterization of the systematic and random measurement errors. The former type of errors is solved by a calibration. Calibration aspects of polarimetric quantities have been intensively studied for both precipitation and cloud radars (Chandrasekar et al., 2015) and are out of the scope of this study. In the case of radar observations of meteorological targets, random errors can be characterized from

measurements if raw (unaveraged) data are available. Cloud radars, however, rarely store raw data because of high data rate. Therefore, commonly used approaches to characterize random errors are based on statistical models of the received radar signals. Random errors of radar signals can be represented by a joint probability density function (PDF) of amplitudes and phases in the two orthogonal polarimetric channels. The joint PDF for polarimetric observations obtained for a single pulse can be found in Middleton (1996, chapter 9.2). Single-pulse measurements, however, are rarely used in the radar meteorology because of the low sensitivity and higher requirement for storage space. The observed radar spectra, almost always, result from the averaging of a number of return pulses. Lee et al. (1994) showed a derivation of a joint probability density function of polarimetric variables for the case of averaging. The authors used a number of assumptions applicable for Earth's surface observations using synthetic-aperture radars. It turns out that the same assumptions are applicable to spectral polarimetric observations of meteorological targets. This allows for using a similar approach in analytic characterization of errors of spectral polarimetric observations.

A number of studies (e.g. Hogan (2007); Cao et al. (2013); Yoshikawa et al. (2014); Chang et al. (2016); Huang et al. (2020)) characterize the joint PDF of polarimetric radar measurements by the error covariance matrix. There are, however, problems with existing approximations of the error covariance matrix for polarimetric observations. First, the elements in the main diagonal of the error covariance matrix – variances of random errors – are found using the first-order Taylor approximation following Bringi and Chandrasekar (2001). Conventional polarimetric variables such as differential reflectivity, correlation coefficient, and differential phase are , however, highly non-linear functions. Therefore, the approximation may lead to biases in the error variance estimates especially when signal-to-noise ratios (SNR) and/or the number of averaged samples is low. This problem becomes important for cloud radars collecting polarimetric variables with a high spatial, temporal, and spectral resolution. Second, non-diagonal components of the error covariance matrix are typically set to zero assuming no correlation between errors in measured quantities but validity and effects of this assumption are not discussed. The information content of measurements is, however, higher when errors are correlated (chapter 3.2.6 in Rodgers, 2000) and therefore, non-negligible off-diagonal elements of the covariance matrix should not be ignored.

This study will review the measurement method of spectral polarimetry with radars operating in the hybrid mode in Sec. 2. In Sec. 3 the likelihood functions of the common polarimetric radar variables are rigorously derived. The error covariance matrix of polarimetric measurements is derived in Sec. 4 by taking into account the correlations among the various measurement random errors. In Sec. 5 the validity of expressions derived for the likelihood functions and error covariance matrix is checked using real raw measurements from a cloud radar.

2 Spectral polarimetry in the hybrid mode

This section introduces known relations between a raw cloud radar signal, complex amplitudes, and spectral polarimetric variables for observations of meteorological targets. These relations are based on the same set of assumptions introduced in classical works of Doviak et al. (1979) and Bringi and Chandrasekar (2001) for precipitation radars.

Since pulsed radars are currently more common in the meteorological community, we use the term "pulse" to refer to a type of the transmitted radar signal in Secs. 2–4. For radars with frequency modulated continuous wave (FMCW) signals, however, the term "chirp" should be used. Later, in the Sec. 5 we use measurements from a FMCW radar and therefore the term "chirp" is used there.

2.1 Complex amplitudes of radar measurements

Radar polarimetric measurements are made in an orthogonal measurement basis defined by feeders of the antenna system. In the hybrid mode the measurement basis is typically Cartesian and formed by the horizontal (h) and vertical (v) components. Further this basis is denoted as the h–v basis. Dual-polarimetric cloud radars have two receivers dedicated to the orthogonal polarimetric components of the received signal. For each transmitted pulse the receivers provide range profiles of in-phase $I_{h,v}$ and quadrature $Q_{h,v}$ components, where indices h and v denote the polarization state. Note, that this study does not cover the radar signal processing to get the $I_{h,v}$ and $Q_{h,v}$ profiles. This information can be found in a radar handbook e.g. Skolnik (2008, Chapter 6). Using N_{fft} profiles of $I_h + iQ_h$ and $I_v + iQ_v$, where i is the imaginary unit, the radar calculates complex Doppler spectra in the horizontal and vertical channel, respectively, applying the Fast Fourier Transformation (FFT) along the time dimension. The complex Doppler spectra are represented by complex amplitudes $\dot{S}$ for each spectral component and each range bin.

Different range bins as well as different spectral components are often considered to be statistically independent, because the corresponding complex amplitudes result from non-coherent scattering of numerous independently moving particles. Some correlation, however, can be expected due to sampling effects and the FFT spectral leakages (e.g. Sec. 5.3 in Marple, 2019). For instance, the power scattered from particles located close to the end of a range bin is distributed between this and the following range bins. These effects depend on filter properties and used FFT windows. It is challenging to give a general analytical solution taking these effects into account. Therefore, these effects are out of the scope of this study. For the sake of simplicity the following analysis is shown only for a single range bin and a single spectral component. Since movements of particles in neighboring range and spectral bins are not related, statistical properties of an individual bin considered in the following are not affected by sampling effects and spectral leakages. The neglection of the dependence of the neighboring bins leads to an underestimation of the information entropy when a complete spectrum and/or spectral profile is analyzed. This worst case assumption, however, allows for a relatively easy and universal characterization of measurement errors. Future studies may improve the error characterization by considering the sampling and leakage effects.

In the following, $\dot{S}_h$ and $\dot{S}_v$ denote the measured complex amplitudes of the analysed spectral component in the horizontal and vertical channels, respectively (the dot hereafter denotes a complex quantity). Introduce a measurement column-vector

$$\hat{\boldsymbol{m}} = [\hat{R}_h, \hat{J}_h, \hat{R}_v, \hat{J}_v]^{\mathrm{T}} \tag{1}$$

with $\hat{R}$ and $\hat{J}$ being real and imaginary parts of a complex amplitude $\dot{S}$, indices h and v denote the polarization state, $^{\mathrm{T}}$ is the transposition sign, the overhat hereafter is used to emphasize measured quantities. The probability density function (PDF) of

$\hat{\boldsymbol{m}}$, given the true covariance matrix $\boldsymbol{\Sigma}_m$ of $\hat{\boldsymbol{m}}$, can be written as follows:

$$f_m\left(\hat{\boldsymbol{m}}|\boldsymbol{\Sigma}_m\right) = (2\pi)^{-2}\det(\boldsymbol{\Sigma}_m)^{-\frac{1}{2}} e^{-\frac{1}{2}\hat{\boldsymbol{m}}^{\mathrm{T}}\boldsymbol{\Sigma}_{\mathbf{m}}\hat{\boldsymbol{m}}}. \tag{2}$$

Note that throughout the study a PDF is a function of measured quantities (e.g. $\hat{\boldsymbol{m}}$ in Eq. 2) with fixed parameters (e.g. $\boldsymbol{\Sigma}_m$ in Eq. 2). The same PDF is called a likelihood function if the measured quantities are fixed and the PDF is viewed as a function of parameters.

Doviak et al. (1979) showed that for meteorological targets I and Q components are jointly normal with zero mean, zero correlation, and equal standard deviation. The authors explain that these properties are due to scattering from a large number of particles moving in an unpredictable way in a scattering volume. Since N_{fft} is much smaller than the number of particles in a resolution volume, the properties are also valid for relations between $\hat{R}_h$ and $\hat{J}_h$ and between $\hat{R}_v$ and $\hat{J}_v$.

The measured complex amplitudes $\dot{S}_h$ and $\dot{S}_v$, however, can be correlated. Taking these properties into account, the true covariance matrix $\boldsymbol{\Sigma}_m$ is defined in the following way (Eq. 5.178 in Bringi and Chandrasekar (2001)):

$$\Sigma_m = \begin{pmatrix} \sigma_h^2 & 0 & q\sigma_h\sigma_v & s\sigma_h\sigma_v \\ 0 & \sigma_h^2 & -s\sigma_h\sigma_v & q\sigma_h\sigma_v \\ q\sigma_h\sigma_v & -s\sigma_h\sigma_v & \sigma_v^2 & 0 \\ s\sigma_h\sigma_v & q\sigma_h\sigma_v & 0 & \sigma_v^2, \end{pmatrix}, \tag{3}$$

where σ_h is the standard deviation of $\hat{R}_h$ and $\hat{J}_h$, σ_v is the standard deviation of $\hat{R}_v$ and $\hat{J}_v$, q is the correlation between $\hat{R}_h$ and $\hat{R}_v$, and s is the correlation between $\hat{R}_h$ and $\hat{J}_v$.

2.2 Polarimetric variables

Unlike precipitation radars which perform rapid azimuth scans, cloud radars are typically pointed to a certain direction or make slow scans to get non-broadened Doppler spectra. Doviak et al. (1979) showed (Eq. 5.2 in there) that the coherency between the adjacent samples depends on the wavelength and the sample repetition period. Cloud radars typically have the pulse repetition frequency in the order of 10 kHz and N_{ftt} in the range from 128 to 1024. This results in getting a single spectrum every 0.01–0.1 s. For such sampling properties of cloud radars any significant coherency between adjacent samples of a spectral line requires the spectral broadening not exceeding at most a few cm s^{-1}. The turbulent spectral broadening, however, exceeds few cm s^{-1} even in stratiform non-precipitating clouds (Borque et al., 2016). Therefore, consecutive samples of complex amplitudes for a spectral line can be considered to be independent.

Since for meteorological targets $\hat{R}_h$ is not correlated with $\hat{J}_h$ and $\hat{R}_v$ is not correlated with $\hat{J}_v$, the absolute phases of $\dot{S}_h$ and $\dot{S}_v$ are uniformly distributed from 0 to 2π and, thus, uninformative. Therefore, the polarimetric observations in the hybrid mode can be represented by a 2×2 covariance matrix $\mathbf{B}$ (Eq. 4.130 in Bringi and Chandrasekar (2001)) instead of the true covariance matrix $\boldsymbol{\Sigma}_m$:

$$\mathbf{B} = \overline{\boldsymbol{e}\boldsymbol{e}^{\mathrm{T}}} = \begin{pmatrix} B_{hh} & \dot{B}_{hv} \\ \dot{B}_{hv}^{*} & B_{vv} \end{pmatrix}, \tag{4}$$

where

$$\boldsymbol{e} = (\dot{S}_h, \dot{S}_v)^{\mathrm{T}}; \tag{5}$$

the overline indicates the expected value, B_{hh} and B_{vv} have meaning of total powers of the horizontal and vertical components of the received signal, respectively, $\dot{B}_{hv}$ is the covariance between the horizontal and vertical components of the received signal, and $*$ is the complex conjugation sign. Note, that in general B_{hh}, B_{vv}, and real and imaginary parts of $\dot{B}_{hv}$ can be calibrated in any quantity that is proportional to the power (Watts) received by the radar; e.g. classical radar reflectivity ($\mathrm{mm}^6\ \mathrm{m}^{-3}$) or even arbitrary units (Myagkov et al., 2016a). Recall, that in this study the covariance matrix $\mathbf{B}$ corresponds to a single spectral component. Such spectral representation of vector signals was introduced by Wiener (1930).

The elements of $\mathbf{B}$ are related to the statistics of the complex amplitudes $\dot{S}_h$ and $\dot{S}_v$ as follows:

$$B_{hh} = \mathrm{var}(\hat{R}_h) + \mathrm{var}(\hat{J}_h) = 2\sigma_h^2, \tag{6}$$

$$B_{vv} = \mathrm{var}(\hat{R}_v) + \mathrm{var}(\hat{J}_v) = 2\sigma_v^2, \tag{7}$$

$$\dot{B}_{hv} = R_{hv} + iJ_{hv} = (q + js)\sigma_h\sigma_v, \tag{8}$$

where R_{hv} and J_{hv} are real and imaginary parts of $\dot{B}_{hv}$.

In the precipitation radar community, dual-polarized measurements are rarely represented by $\mathbf{B}$. Instead a set of polarimetric variables is used. Therefore, the same polarimetric variables (but spectrally resolved) are introduced in this study. Introduce a vector

$$\boldsymbol{c} = (B_{hh}, Z_{DR}, \rho_{HV}, \Phi_{DP})^T, \tag{9}$$

where Z_{DR} is the differential reflectivity, ρ_{HV} is the correlation coefficient, and Φ_{DP} is the differential phase. In this study Z_{DR}, ρ_{HV}, and Φ_{DP} are defined for each spectral line using elements of corresponding $\mathbf{B}$:

$$Z_{DR} = \frac{B_{hh}}{B_{vv}}, \tag{10}$$

$$\rho_{HV} = \sqrt{\frac{R_{hv}^2 + J_{hv}^2}{B_{hh}B_{vv}}}, \tag{11}$$

$$\Phi_{DP} = \mathrm{atan}\left(-\frac{J_{hv}}{R_{hv}}\right). \tag{12}$$

Note, that elements of the matrix $\mathbf{B}$ are in general affected by noise. The noise in both polarimetric channels is not known exactly. Typically, it is estimated from spectra using e.g. the algorithm from Hildebrand and Sekhon (1974). A subtraction of noise levels from corresponding diagonal terms of the covariance matrix $\mathbf{B}$ to get an estimate of signal-only powers leads to occasions when the covariance matrix is no longer positive semi-definite. In this case, ρ_{HV} calculated from the noise corrected covariance matrix can exceed 1, which is beyond the range of valid values. In order to avoid this problem, we characterize radar measurements without noise subtraction. A further advantage of this approach is that spectral lines containing noise only can also be correctly characterized.

3 Likelihood of elements of the covariance matrix B

Assume the following problem. The state of the atmosphere is represented by the state vector $\boldsymbol{x}$. A forward model F maps $\boldsymbol{x}$ into a vector

$$F(\boldsymbol{x}) = \boldsymbol{b} = (B_{hh}, R_{hv}, J_{hv}, B_{vv})^{\mathrm{T}} \tag{13}$$

in the space of observations. The actual measurement vector is

$$\hat{\boldsymbol{b}} = (\hat{B}_{hh}, \hat{R}_{hv}, \hat{J}_{hv}, \hat{B}_{vv})^{\mathrm{T}} = \boldsymbol{b} + \boldsymbol{\epsilon}, \tag{14}$$

where

$$\hat{B}_{hh} = \left\langle \dot{S}_h \dot{S}_h^* \right\rangle, \tag{15}$$

$$\hat{R}_{hv} = \mathrm{Re}\left(\left\langle \dot{S}_h \dot{S}_v^* \right\rangle \right), \tag{16}$$

$$\hat{J}_{hv} = \mathrm{Im}\left(\left\langle \dot{S}_h \dot{S}_v^* \right\rangle \right), \tag{17}$$

$$\hat{B}_{vv} = \left\langle \dot{S}_v \dot{S}_v^* \right\rangle, \tag{18}$$

are constituents of the measured covariance matrix $\hat{\mathbf{B}}$ and $\boldsymbol{\epsilon}$ represents the vector of measurement random errors in each component of $\hat{\boldsymbol{b}}$. In Eqs. 15–18 Re and Im are the real and imaginary parts of a complex number. <> denotes averaging over N_s independent complex spectra calculated from non-overlapping time sequences. The estimators Eqs. 15–18 are the same as given in Bringi and Chandrasekar (2001, Chapter 6.4.5). The only difference is that within this work the variables are calculated using complex amplitudes for a spectral line instead of using I/Q components as is done by precipitation radars. What is the likelihood of $\hat{\boldsymbol{b}}$ given the state vector $\boldsymbol{x}$? In the case the forward model provides a unique and accurate relation between $\boldsymbol{x}$ and $\boldsymbol{b}$, the problem is equivalent to finding $f_b(\hat{\boldsymbol{b}}|\boldsymbol{b}, N_s)$ – the likelihood of $\hat{\boldsymbol{b}}$ – given the true vector of measurements $\boldsymbol{b}$ and the number of averaged spectra N_s. The derivation of $f_b(\hat{\boldsymbol{b}}|\boldsymbol{b}, N_s)$ provided in this section includes several steps. In Sec. 3.1 the polarimetric basis is changed to cancel the correlations between the orthogonal components of the measured vector. In the new basis the likelihood function can be represented by a product of likelihood functions, each of which is a function of only a single independent element. In Sec. 3.2 a formal derivation of the likelihood function in this new basis is provided. The solution for $f_b(\hat{\boldsymbol{b}}|\boldsymbol{b}, N_s)$ is given in Sec. 3.3 converting back to the original space and applying the rule of change of variables. As it was mentioned above, the radar observations are often represented by the vector $\boldsymbol{c}$. Therefore, Sec. 3.3 also provides the likelihood $f_c(\hat{\boldsymbol{c}}|\boldsymbol{b}, N_s)$.

3.1 Diagonalization of the covariance matrix B

As it was previously mentioned, $\dot{S}_h$ and $\dot{S}_v$ are, in general, correlated. There is, however, always a basis, in which the projections of $\dot{S}_h$ and $\dot{S}_v$ become completely uncorrelated. This basis is further denoted as the c–x (co-polar and cross-polar) basis.

The conversion of the vector $\boldsymbol{e}$ in the h–v basis to the vector $\boldsymbol{e}_D$ in c–x basis is made using the unitary operator $\mathbf{Q}$:

$$\boldsymbol{e}_D = \begin{pmatrix} \dot{S}_c \\ \dot{S}_x \end{pmatrix} = \mathbf{Q}\boldsymbol{e} \tag{19}$$

The calculation of the matrix $\mathbf{Q}$ is given in Appendix A. Real and imaginary parts of $\dot{S}_c$ are jointly distributed normally with the zero mean, zero correlation, and standard deviation σ_c. Real and imaginary parts of $\dot{S}_x$ are also jointly distributed normally with zero mean, zero correlation, but have, in general, a different standard deviation σ_x.

The covariance matrix $\mathbf{D}$ of $\boldsymbol{e}_D$ has the diagonal form and can be found as follows

$$\mathbf{D} = \begin{pmatrix} D_{cc} & 0 \\ 0 & D_{xx} \end{pmatrix} = \mathbf{Q}^{\dagger}\mathbf{B}\mathbf{Q}. \tag{20}$$

In Eq. 20 † is the Hermitian conjugate. The elements of the matrix $\mathbf{D}$ can be found as follows:

$$D_{cc} = q_{11}^2 B_{hh} + |\dot{q}_{12}|^2 B_{vv} - 2q_{11}\left(R_{12}R_{hv} + J_{12}J_{hv}\right) \tag{21}$$

$$D_{xx} = |\dot{q}_{12}|^2 B_{hh} + q_{11}^2 B_{vv} + 2q_{11}\left(R_{12}R_{hv} + J_{12}J_{hv}\right) \tag{22}$$

where $\dot{q}_{nm}$ are elements of $\mathbf{Q}$ with n and m being indices of row and column, respectively;

$$\dot{q}_{12} = R_{12} + iJ_{12}. \tag{23}$$

Similar to relations between the powers and the standard deviations given in Eqs. 6 and 44, σ_1 and σ_2 are related to D_{cc} and D_{xx}, respectively:

$$D_{cc} = \text{var}(R_c) + \text{var}(J_c) = 2\sigma_c^2 \tag{24}$$

$$D_{xx} = \text{var}(R_x) + \text{var}(J_x) = 2\sigma_x^2 \tag{25}$$

The measured values $\hat{D}_{cc}$,

$$\hat{D}_{cx} = \hat{R}_{cx} + i\hat{J}_{cx}, \tag{26}$$

and $\hat{D}_{xx}$ represent elements of the matrix $\hat{\mathbf{D}}$:

$$\hat{\mathbf{D}} = \mathbf{Q}^{\dagger}\hat{\mathbf{B}}\mathbf{Q}. \tag{27}$$

Note, that the operator $\mathbf{Q}$ is the same as in Eq. 20 and not recalculated using $\hat{\mathbf{B}}$.

3.2 Likelihood function in the c–x basis

By definition, the off-diagonal elements of the covariance matrix $\mathbf{D}$ are zeros (see Eq. 20). This implies no correlation between $\dot{S}_c$ and $\dot{S}_x$. In this case, the likelihood function $f_d(\hat{\boldsymbol{d}}|\boldsymbol{b}, N_s)$, where

$$\hat{\boldsymbol{d}} = (\hat{D}_{cc}, \hat{R}_{cx}, \hat{J}_{cx}, \hat{D}_{xx})^{\mathrm{T}}, \tag{28}$$

can be written as a multiplication of likelihood functions of individual components:

$$f_d(\hat{\boldsymbol{d}}|\boldsymbol{b},N_s) = f(\hat{D}_{cc}|\boldsymbol{b},N_s)f(\hat{R}_{cx}|\boldsymbol{b},N_s)f(\hat{J}_{cx}|\boldsymbol{b},N_s)f(\hat{D}_{xx}|\boldsymbol{b},N_s). \tag{29}$$

PDFs of the individual components can be found as follows:

$$f\left(\hat{D}_{cc}|\boldsymbol{b},N_s\right) = \frac{N_s}{\sigma_c^2}\chi^2_{2N_s}\left(\frac{N_s}{\sigma_c^2}\hat{D}_{cc}\right), \tag{30}$$

$$f\left(\hat{D}_{xx}|\boldsymbol{b},N_s\right) = \frac{N_s}{\sigma_x^2}\chi^2_{2N_s}\left(\frac{N_s}{\sigma_x^2}\hat{D}_{xx}\right), \tag{31}$$

$$f\left(\hat{R}_{cx}|\boldsymbol{b},N_s\right) = \frac{(2N_s)^a|\hat{R}_{cx}|^{-b}}{\sqrt{\pi}2^{2N_s}(\sigma_c\sigma_x)^a\Gamma(N_s)}K_b\left(\frac{|2N_s\hat{R}_{cx}|}{\sigma_c\sigma_x}\right), \tag{32}$$

$$f\left(\hat{J}_{cx}|\boldsymbol{b},N_s\right) = \frac{(2N_s)^a|\hat{J}_{cx}|^{-b}}{\sqrt{\pi}2^{2N_s}(\sigma_c\sigma_x)^a\Gamma(N_s)}K_b\left(\frac{|2N_s\hat{J}_{cx}|}{\sigma_c\sigma_x}\right), \tag{33}$$

where χ^2_k is the chi-squared distribution with k degrees of freedom,

$$a = (2N_s+1)/2, \tag{34}$$

$$b = (1-2N_s)/2, \tag{35}$$

Γ is the gamma function, and K_μ is the Bessel function of the second kind of order μ. Recall, that σ_c and σ_x in Eqs. 30–33 are derived from the elements of $\boldsymbol{b}$ using Eqs. 21–22 and Eqs 24 and 25. Derivation and Monte Carlo evaluation of Eqs. 30–33 is given in Appendix B. Appendix B3 shows how to handle Eqs. 32 and 33 when $\hat{R}_{cx}$ and $\hat{J}_{cx}$ are close to 0.

3.3 Likelihood function in the h–v basis

Applying the rule of changing variables in a multivariate PDF (e.g. Walpole et al., 2012, Theorem 7.4) $f_b(\hat{\boldsymbol{b}}|\boldsymbol{b},N_s)$ can be found from Eqs. 29 as follows:

$$f_b(\hat{\boldsymbol{b}}|\boldsymbol{b},N_s) = f_d(\hat{\boldsymbol{d}}|\boldsymbol{b},N_s). \tag{36}$$

As shown in Appendix B5, the determinant of the Jacobian of the transformation from $\hat{\boldsymbol{b}}$ to $\hat{\boldsymbol{d}}$ is equal to 1.

Likelihood $f_c(\hat{\boldsymbol{c}}|\boldsymbol{b},N_s)$ of a vector

$$\hat{\boldsymbol{c}} = (\hat{B}_{hh},\hat{Z}_{DR},\hat{\rho}_{HV},\hat{\Phi}_{DP}) \tag{37}$$

can be found by multiplying $f_b(\hat{\boldsymbol{b}}|\boldsymbol{b},N_s)$ by $|\mathbf{J}_{cb}|$ with

$$\mathbf{J}_{cb} = -B^3_{hh}Z^{-3}_{DR}\rho_{HV} \tag{38}$$

being the Jacobian of the transformation from $\hat{\boldsymbol{c}}$ to $\hat{\boldsymbol{b}}$ (see Appendix B6):

$$f_c(\hat{\boldsymbol{c}}|\boldsymbol{b},N_s) = B^3_{hh}Z^{-3}_{DR}\rho_{HV}f_b(\hat{\boldsymbol{b}}|\boldsymbol{b},N_s). \tag{39}$$

Equations 36, and 39 can be used for the maximum likelihood optimization and Bayesian inference methods. Ready-to-use MATLAB implementations of these equations are provided in the supplement.

4 Error covariance matrices

A number of problems such as optimal estimation, data assimilation, and sensitivity analysis require the covariance matrix of the measurement errors. Unfortunately, an analytical integration of Eqs. 29, 36, and 39 required for the statistical moment calculation is challenging. In this section, however, known relations for calculation of variances and covariances after a linear transformation are used.

4.1 Error covariance matrix of b

The covariance matrix $\hat{\mathbf{B}}$ estimated from measurements is related to the matrix $\hat{\mathbf{D}}$ as follows:

$$\hat{\mathbf{B}} = \mathbf{Q}\hat{\mathbf{D}}\mathbf{Q}^{\dagger}. \tag{40}$$

Therefore, the elements of the vector $\hat{\boldsymbol{b}}$ can be found as linear combinations of the elements of the vector $\hat{\boldsymbol{d}}$:

$$\hat{B}_{hh} = q_{11}^2 \hat{D}_{cc} + |\dot{q}_{12}|^2 \hat{D}_{xx} + 2q_{11}\left(R_{12}\hat{R}_{cx} + J_{12}\hat{J}_{cx}\right), \tag{41}$$

$$\hat{R}_{hv} = q_{11}R_{12}\left(\hat{D}_{xx} - \hat{D}_{cc}\right) + \left(q_{11}^2 - R_{12}^2 + J_{12}^2\right)\hat{R}_{cx} - 2R_{12}J_{12}\hat{J}_{cx} \tag{42}$$

$$\hat{J}_{hv} = q_{11}J_{12}\left(\hat{D}_{xx} - \hat{D}_{cc}\right) + \left(q_{11}^2 + R_{12}^2 - J_{12}^2\right)\hat{J}_{cx} - 2R_{12}J_{12}\hat{R}_{cx} \tag{43}$$

$$\hat{D}_{vv} = |\dot{q}_{12}|^2 \hat{D}_{cc} + q_{11}^2 \hat{D}_{xx} - 2q_{11}\left(R_{12}\hat{R}_{cx} + J_{12}\hat{J}_{cx}\right), \tag{44}$$

or in matrix form:

$$\hat{\boldsymbol{b}} = \begin{pmatrix} q_{11}^2 & 2q_{11}R_{12} & 2q_{11}J_{12} & |\dot{q}_{12}|^2 \\ -q_{11}R_{12} & q_{11}^2 - R_{12}^2 + J_{12}^2 & -2R_{12}J_{12} & q_{11}R_{12} \\ -q_{11}J_{12} & -2R_{12}J_{12} & q_{11}^2 + R_{12}^2 - J_{12}^2 & q_{11}J_{12} \\ |\dot{q}_{12}|^2 & -2q_{11}R_{12} & -2q_{11}J_{12} & q_{11}^2 \end{pmatrix} \hat{\boldsymbol{d}} = \mathbf{M}\hat{\boldsymbol{d}}. \tag{45}$$

In this case, as shown in Wilks D.S. (chapter 10.4.3), the error covariance matrix Σ_b of $\hat{\boldsymbol{b}}$ can be calculated from the error covariance matrix Σ_d of $\hat{\boldsymbol{d}}$:

$$\Sigma_b = \mathbf{M}\Sigma_d\mathbf{M}^T, \tag{46}$$

where

$$\Sigma_d = \begin{pmatrix} 4\sigma_c^4/N_s & 0 & 0 & 0 \\ 0 & \sigma_c^2\sigma_x^2/N_s & 0 & 0 \\ 0 & 0 & \sigma_c^2\sigma_x^2/N_s & 0 \\ 0 & 0 & 0 & 4\sigma_x^4/N_s \end{pmatrix} \tag{47}$$

The off-diagonal terms of Σ_d are set to 0 taking into account that the elements of $\hat{\boldsymbol{d}}$ are not correlated. The derivation of diagonal terms – variances of elements of $\hat{\boldsymbol{d}}$ – is given in Appendix C. A ready-to-use MATLAB implementation of Eq. 46 is provided in the supplement.

4.2 Error covariance matrix of $\boldsymbol{c}$

As it was shown in Sec. 4.1, the error covariance matrix Σ_b can be used to characterize uncertainties of spectral radar observations. In this study, however, the error covariance of the vector $\hat{\boldsymbol{c}}$ is also obtained. It will be further demonstrated that a representation of measurement uncertainties for $\hat{\boldsymbol{c}}$ is deficient.

Recall that the calculation of $\hat{\boldsymbol{c}}$ includes highly nonlinear functions. Therefore, the error covariance matrix Σ_c of the vector $\hat{\boldsymbol{c}}$ is estimated using the first-order Taylor approximation. Bringi and Chandrasekar (2001) used a similar approach to calculate variances of polarimetric variables.

$$\Sigma_c = \mathbf{S}\Sigma_b\mathbf{S}^T, \tag{48}$$

where $\mathbf{S}$ is the sensitivity matrix:

$$\mathbf{S} = \begin{pmatrix} \frac{\partial B_{hh}}{\partial B_{hh}} & \frac{\partial B_{hh}}{\partial R_{hv}} & \frac{\partial B_{hh}}{\partial J_{hv}} & \frac{\partial B_{hh}}{\partial B_{vv}} \\ \frac{\partial Z_{DR}}{\partial B_{hh}} & \frac{\partial Z_{DR}}{\partial R_{hv}} & \frac{\partial Z_{DR}}{\partial J_{hv}} & \frac{\partial Z_{DR}}{\partial B_{vv}} \\ \frac{\partial \rho_{HV}}{\partial B_{hh}} & \frac{\partial \rho_{HV}}{\partial R_{hv}} & \frac{\partial \rho_{HV}}{\partial J_{hv}} & \frac{\partial \rho_{HV}}{\partial B_{vv}} \\ \frac{\partial \Phi_{DP}}{\partial B_{hh}} & \frac{\partial \Phi_{DP}}{\partial R_{hv}} & \frac{\partial \Phi_{DP}}{\partial J_{hv}} & \frac{\partial \Phi_{DP}}{\partial B_{vv}} \end{pmatrix} \tag{49}$$

Substituting Eqs. 10 – 12 into Eq. 49

$$\mathbf{S} = \begin{pmatrix} 1 & 0 & 0 & 0 \\ B_{vv}^{-1} & 0 & 0 & -B_{hh}B_{vv}^{-2} \\ -0.5|\dot{B}_{hv}|B_{vv}^{-0.5}B_{hh}^{-1.5} & R_{hv}|\dot{B}_{hv}|^{-1}(B_{hh}B_{vv})^{-0.5} & J_{hv}|\dot{B}_{hv}|^{-1}(B_{hh}B_{vv})^{-0.5} & -0.5|\dot{B}_{hv}|B_{hh}^{-0.5}B_{vv}^{-1.5} \\ 0 & -J_{hv}|\dot{B}_{hv}|^{-2} & R_{hv}|\dot{B}_{hv}|^{-2} & 0 \end{pmatrix}. \tag{50}$$

A ready-to-use MATLAB implementation of Eq. 48 is provided in the supplement.

5 Consistency checks on radar observations

In order to check consistency of Eqs. 36, 39, 46 and 48 with radar measurements, I/Q data collected with a W-band cloud radar with the hybrid polarimetric mode were used (Myagkov and Unal, 2021). The radar is a part of a dual-frequency system owned and operated by the Technical University of Delft in Cabauw, the Netherlands. Technical specifications of the radar can be found in Myagkov et al. (2020). The radar uses frequency modulated continuous signals. Küchler et al. (2017) explain the operation principle and shows that the radar profiles the atmosphere using several chirp types. Each chirp type is dedicated to a certain distance range. During measurements chirp types are switched consequently. For each chirp type a number of chirps (chirp sequence hereafter) is processed continuously. Operational settings used during I/Q measurements are listed in Table 1.

Measurements were made during a rain event on 21 June 2021 at 7:44 UTC. I/Q measurements provide high data rate of about 900 MB min^{-1}. Therefore, about 3 min of I/Q measurements were collected for the analysis. The radar was pointed

Table 1. Operational setting of the used W-band radar

Parameter	Chirp type 1	Chirp type 2	Chirp type 3
Covered distance [km]	0.1–1.2	1.2–4.9	4.9–15
Range resolution [m]	29.8	29.8	55
Number of chirps in a sequence	7168	7168	9216
Chirp repetition frequency [kHz]	9.2	7.5	5

to 45° elevation. Since different chirp types have different properties, in the following only I/Q data collected with the first chirp type are used. Since the first chirp sequence covers the lowest part of the atmosphere, the analyzed data correspond to rain. As explained in Sec. 2, no noise subtraction is required to describe the statistics of the measurements. We therefore, use all available spectral lines, including those containing noise only. 90% of spectral noise power was from 0.2–1.3$\times 10^{-3}$ [a.u]. Signal-to-noise ratio (defined here as a ratio of signal power in a spectral line divided by the mean spectral noise power in the same range bin) specified in linear units was from 0 (no signal) to 10^6. We would like to emphasize, that no filtering based on signal-to-noise ratio was applied. Taking into account that the first chirp type has 37 range bins, in total 2.2×10^3 chirp sequences (15.9×10^6 chirps) are available in each polarimetric channel.

5.1 Processing

All I/Q measurements within a chirp sequence in every polarimetric channel are split into 224 continuous blocks. Each block contains 32 I/Q pairs. The FFT with the Blackman weighting window is applied to each block to get complex Doppler spectra. Then the 224 blocks are split into 28 sub-blocks with 8 spectra in each sub-block. Within each sub-block elements of the vector $\hat{\boldsymbol{b}}$ are calculated according to Eqs. 15–18 with $N_s = 8$ for every spectral line. For each $\hat{\boldsymbol{b}}$ the vector $\hat{\boldsymbol{c}}$ is obtained. Note, that for this Eqs. 10–12 were applied to elements of $\hat{\boldsymbol{b}}$ instead of $\boldsymbol{b}$. Using vectors $\hat{\boldsymbol{b}}$ and $\hat{\boldsymbol{c}}$ within a sequence the error covariance matrices $\hat{\Sigma}_b$ and $\hat{\Sigma}_c$ are calculated numerically. The overhat here indicate that the error covariance matrices are estimated from measurements.

The calculation of the likelihood functions using Eqs. 36 and 39 require $\boldsymbol{b}$. The approximation of covariance matrices using Eqs. 46 and 48 requires the matrix $\mathbf{B}$. In order to estimate $\boldsymbol{b}$ and $\mathbf{B}$, elements of the vector $\hat{\boldsymbol{b}}$ are averaged over 28 sub-blocks available within a single chirp sequence. These averaged values are assumed to be elements of the vector $\boldsymbol{b}$ from which the matrix $\mathbf{B}$ is obtained. Using $\mathbf{B}$ and $N_s = 8$, Σ_b and Σ_c are calculated for each chirp sequence as shown in Fig. 1.

5.2 Filtering

The random error analysis provided in this study is only applicable to volume-distributed scattering and noise. As discussed in Sec. 2, in this case $\hat{R}_h$ is not correlated with $\hat{J}_h$ and $\hat{R}_v$ is not correlated with $\hat{J}_v$. However, radar observations in general contain scattering from atmospheric plankton, ground clutter, and coherent receiver noise, which do not fulfil the assumption.

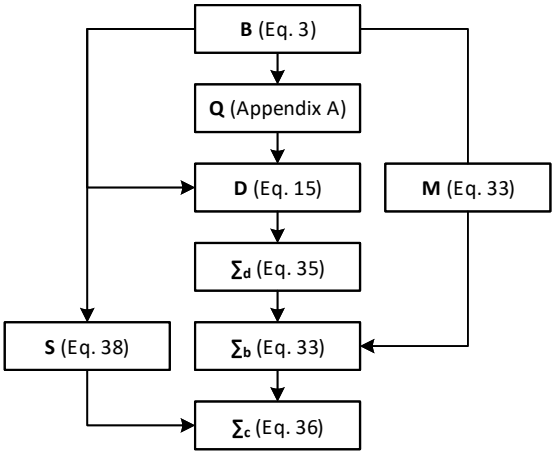

Figure 1. Schematic illustration of the error covariance matrix calculation.

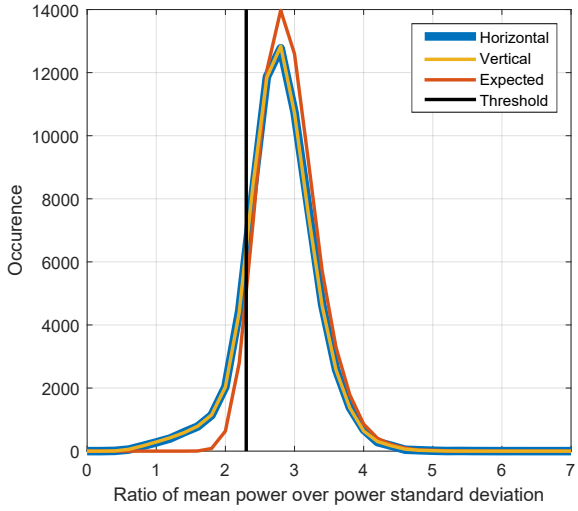

Figure 2. Distributions of the ratio of mean power over the power standard deviation for the horizontal (blue line) and vertical (yellow line) channels. The expected distribution is shown with the red line. The black vertical line indicates the threshold corresponding to the 5th percentile of the distribution for the randomly generated complex numbers.

330 In order to filter out spectral lines with correlated real and imaginary parts, a simple filtering rule was applied. It is known, that for a signal with uncorrelated in-phase and quadrature components, its mean power and power standard deviation are related to each other (Eq. 5.193 in Bringi and Chandrasekar, 2001). Figure 2 shows distributions of the mean power over the power standard deviation calculated in the horizontal and vertical polarization channels shown by blue and yellow lines,

respectively. It can be seen that the mode of the distributions is close to the theoretical value of $\sqrt{N_s} = 2.8$. The distributions, however, have a considerable tail on the left side. These small values of the ratio are expected for correlated in-phase and quadrature components. Thus, a threshold in the ratio of the mean power over the standard deviation of power can be used to filter out unwanted spectral lines. In order to specify the threshold, the Monte Carlo approach was used. 15.9×10^6 random complex values with normal distribution, zero mean, and the standard deviation of 1 were generated. The same processing as for measured I/Q data was applied to the generated complex values. The distribution of the ratio of the mean power over the power standard deviation for the generated data (denoted as expected distribution) is shown in Fig. 2 by the red line. The expected distribution has much smaller tail on the left side relative to the ones of the measured distributions. The threshold of 2.3 used for filtering is chosen as the 5th percentile of the expected distribution. Vectors $\hat{\boldsymbol{b}}$ and $\hat{\boldsymbol{c}}$ are excluded from the analysis if for the corresponding spectral component within a chirp sequence the ratio of the mean power over the power standard deviation is below the threshold in at least one of the polarimetric channels. The amount of excluded data is about 18 %.

5.3 Evaluation of $f_b(\hat{\boldsymbol{b}}|\boldsymbol{b}, \boldsymbol{N_s})$ and $f_b(\hat{\boldsymbol{c}}|\boldsymbol{b}, \boldsymbol{N_s})$

Recall, that $\boldsymbol{b}$ is estimated from measurements by averaging all available sub-blocks within a chirp sequence. $\boldsymbol{b}$, however, can also be estimated by maximization of the likelihood functions given in Eqs. 36 and 39. In this case, an optimization algorithm needs to be employed to find a set of elements of $\boldsymbol{b}$ corresponding to the global maximum in either Eq. 36 or Eq. 39. This study uses a derivative-free optimization method available by default in MATLAB (Lagarias et al., 1998). Since the optimization method minimizes a function, the likelihood functions were not used directly. Instead, the following cost functions were used for the minimization:

$$C_b = -\sum_{l=1}^{28} \log_{10}(f_b(\hat{\boldsymbol{b}}|\boldsymbol{b}, N_s)), \tag{51}$$

$$C_c = -\sum_{l=1}^{28} \log_{10}(f_c(\hat{\boldsymbol{c}}|\boldsymbol{b}, N_s)). \tag{52}$$

Here the index l runs over 28 sub-blocks within a chirp sequence. Equations 51 and 52 take into account that the consecutive $\hat{\boldsymbol{b}}$ are not correlated. In this case the total likelihood of 28 vectors $\hat{\boldsymbol{b}}$ is a product of likelihood of each individual $\hat{\boldsymbol{b}}$. In order to avoid an overflow of double numbers, the logarithm was used. In this case the logarithm of the product is replaced by the sum of logarithms. The logarithm is monotonically increasing function and, therefore, it does not change the position of the maximum of the likelihood function. Finally, the minus sign was introduced to have a smaller value of a cost function corresponding to a higher value of the likelihood. For the evaluation, 1000 chirp sequences were chosen randomly for the maximum likelihood estimation using $f_b(\hat{\boldsymbol{b}}|\boldsymbol{b}, N_s)$. In each chirp sequence a single spectral line was randomly chosen for the analysis. Thus, there are 28 vectors $\hat{\boldsymbol{b}}$ available in each of the 1000 chirp sequences. For each sequence, the optimization algorithm requires an initial guess of $\boldsymbol{b}$. In order to avoid local minima, 5 different initial guesses were used, which are a coefficient P multiplied by the first $\hat{\boldsymbol{b}}$ in the analyzed chirp sequence. The values of P were 0.5, 0.75, 1, 1.25, and 1.5. The solution giving the lowest cost function out of the 5 outcomes was chosen as the result. Similarly the maximum likelihood estimation using $f_c(\hat{\boldsymbol{c}}|\boldsymbol{b}, N_s)$ was done using

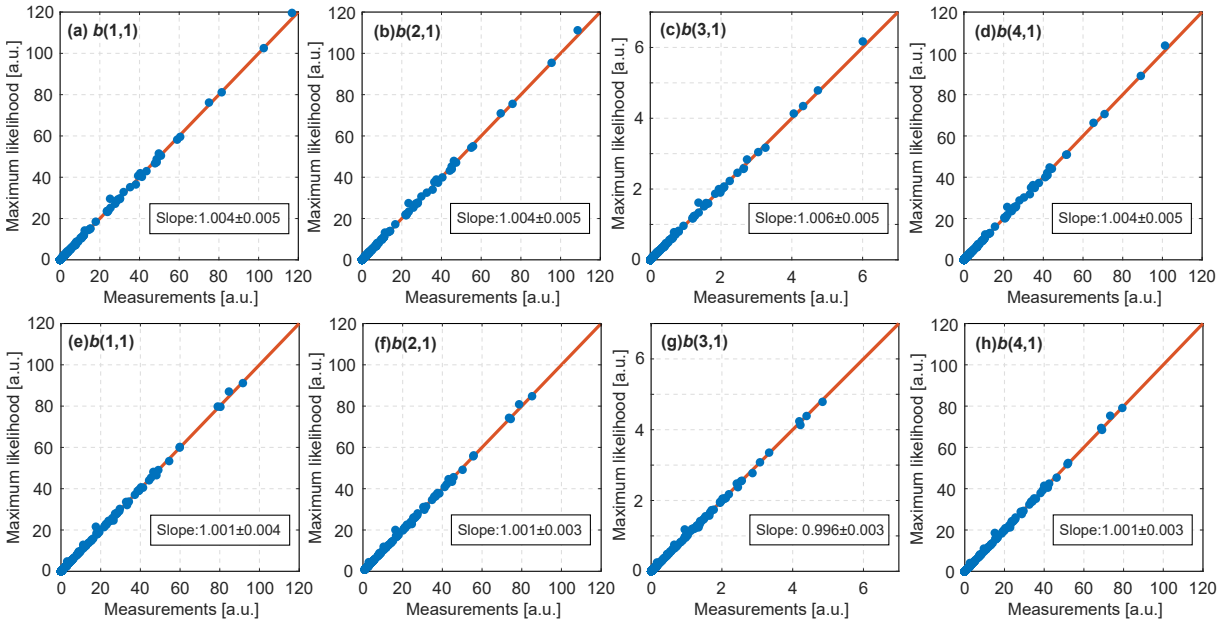

Figure 3. Comparison of elements of $\boldsymbol{b}$ estimated by the averaging over 28 sub-blocks (x-axis) with those estimated by the maximum likelihood approach (y-axis). $f_b(\hat{\boldsymbol{b}}|\boldsymbol{b}, N_s)$ was used for panels (a)–(d). $f_c(\hat{\boldsymbol{c}}|\boldsymbol{b}, N_s)$ was used for panels (e)–(h). Each panel contains 1000 points described in text. Linear regressions are shown by red solid lines. Each panel has a text box with the slope of the corresponding linear regression. Uncertainties of the slopes were estimated using the bootstrapping. Note, that units are not critical for the evaluation of the correctness of the derived likelihood functions. Therefore, arbitrary units (a.u) are used.

independently chosen 1000 chirp sequences. Figure 3 shows a comparison of elements of $\boldsymbol{b}$ estimated by the averaging over 28 sub-blocks and those estimated by the maximum likelihood approach. All panels show a good agreement indicated by the close-to-unity slope of the linear regression. Both $f_b(\hat{\boldsymbol{b}}|\boldsymbol{b}, N_s)$ (results in the first row of Fig. 3) and $f_c(\hat{\boldsymbol{c}}|\boldsymbol{b}, N_s)$ (results in the second row of Fig. 3) show the same level of agreement and, therefore, can be used with no difference.

5.4 Evaluation of Σ_c

Diagonal elements of Σ_c – variances of $\hat{B}_{hh}$, $\hat{Z}_{DR}$, $\hat{\rho}_{HV}$, and $\hat{\Phi}_{DP}$ – were checked against those calculated using Eqs. 6.139a, 6.141, 6.144, and 6.143 in Bringi and Chandrasekar (2001), respectively. Taking into account, that samples for a spectral line are not correlated, approximations for variances of $\hat{B}_{hh}$, $\hat{Z}_{DR}$, $\hat{\rho}_{HV}$, and $\hat{\Phi}_{DP}$ based on the equations in Bringi and Chandrasekar (2001) are:

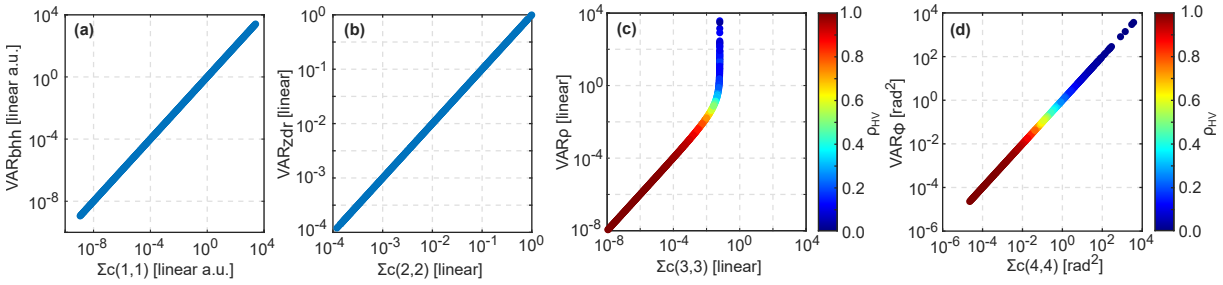

Figure 4. Comparison of variances of (a) $\hat{B}_{hh}$, (b) $\hat{Z}_{DR}$, (c) $\hat{\rho}_{HV}$, and (d) $\hat{\Phi}_{DP}$. Approximations developed in this study are on the x-axis. Approximations from Bringi and Chandrasekar (2001) are on the y-axis. ρ_{HV} is color-coded in panels (c) and (d) to illustrate at which values of ρ_{HV} approximations lead to erroneous values (see details in text). Note, that units are not critical for the evaluation of the derived equations. Therefore, arbitrary units (a.u) are used in the panel (a).

$$\mathrm{VAR}_{bhh} = \frac{B_{hh}^2}{N_s}, \tag{53}$$

$$\mathrm{VAR}_{zdr} = \frac{2Z_{DR}^2(1-\rho_{HV}^2)}{N_s}, \tag{54}$$

$$\mathrm{VAR}_{\rho} = \frac{(1-\rho_{HV}^2)^2}{2N_s\rho_{HV}^2}, \tag{55}$$

$$\mathrm{VAR}_{\Phi} = \frac{(1-\rho_{HV}^2)}{2N_s\rho_{HV}^2}, \tag{56}$$

$$\tag{57}$$

respectively.

Figure 4 shows that VAR_{bhh}, VAR_{zdr}, and VAR_{Φ} match exactly $\Sigma_c(1,1)$, $\Sigma_c(2,2)$, and $\Sigma_c(4,4)$, respectively. VAR_{ρ}, however, agrees with $\Sigma_c(3,3)$ only at values of $\rho_{HV} > 0.95$. Below this value VAR_{ρ} overestimates the variance of $\hat{\rho}_{HV}$. At values of ρ_{HV} close to 0, VAR_{ρ} has unrealistically high values, which result from ρ_{HV} in the denominator of Eq. 55.

Figure 4d also shows unrealistic values with both approximations of the $\hat{\Phi}_{DP}$ variance. Taking into account that $\hat{\Phi}_{DP}$ can take values within the range from 0 to 2π rad, the variance of $\hat{\Phi}_{DP}$ exceeding 10^3 rad^2 is definitely erroneous. The high variance of $\hat{\Phi}_{DP}$ corresponds to values of $\rho_{HV} < 0.3$. This effect results from the first-order Taylor approximation of Eq. 12 which is a highly non-linear function.

A comparison of the error covariance matrices $\hat{\Sigma}_c$ with the calculated one Σ_c is shown in Fig. 5. Panels (f), (k), and (p) indicate considerable differences caused by the first-order Taylor approximation in variances of $\hat{Z}_{DR}$, $\hat{\rho}_{HV}$, and $\hat{\Phi}_{DP}$, respectively. The results also reveal that the first-order Taylor approximation cannot adequately represent most of the non-diagonal components of the error covariance matrix.

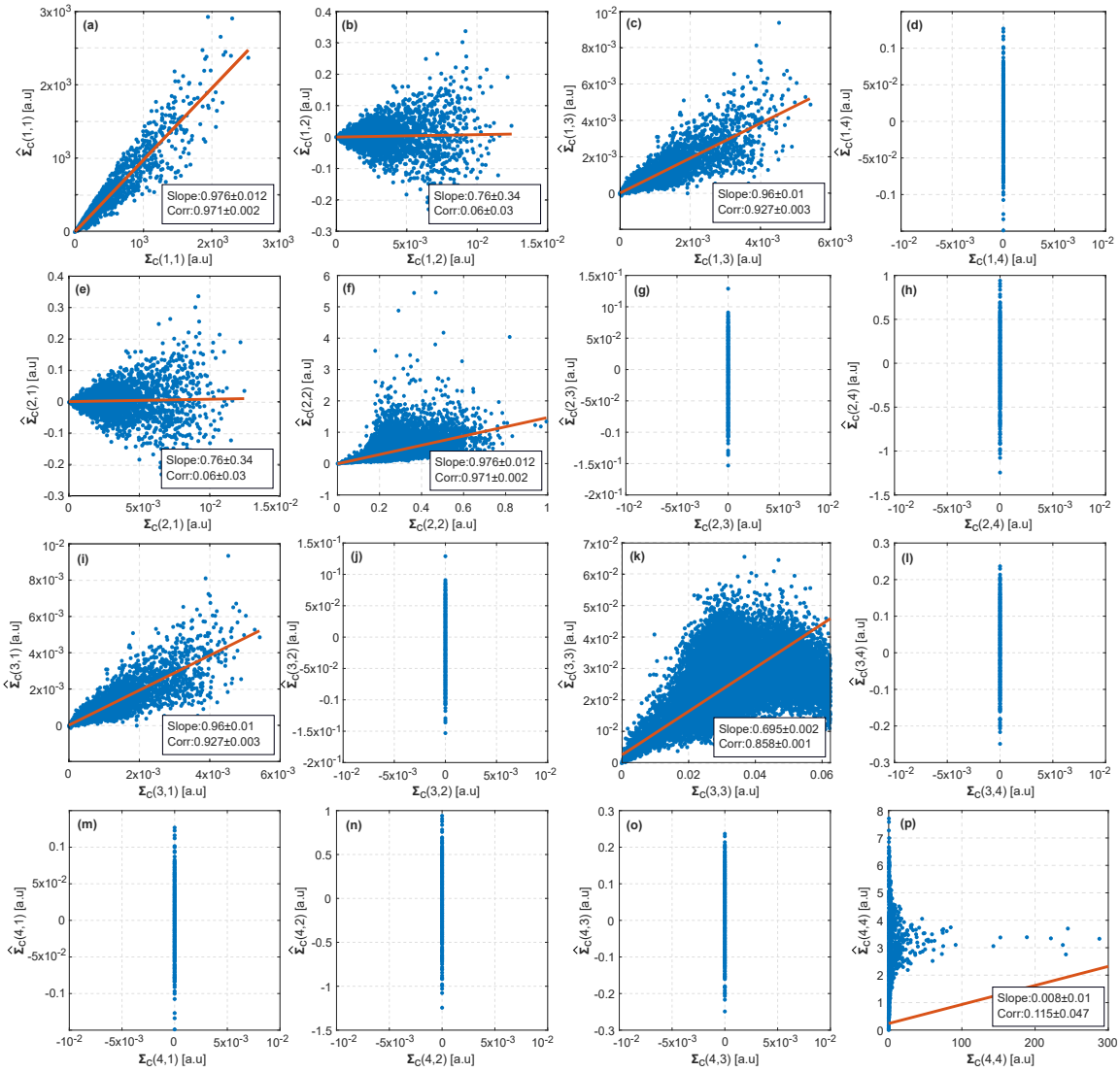

Figure 5. Comparison of $\hat{\Sigma}_c$ estimated from the radar measurements with Σ_c obtained from Eq. 48. Elements of Σ_c are given on the x-axes. Elements of $\hat{\Sigma}_c$ are given on the y-axes. The first and the second numbers in brackets indicate the row and the column of the corresponding matrix, respectively. Linear regressions are shown by red lines. Slopes of the linear regressions and Pearson correlations are given in boxes in each panel. Uncertainties in the slope and the correlation are represented by $\pm$ one standard deviation of the corresponding parameter. The standard deviations are obtained using the bootstrapping. Panels without linear regressions show elements for which Eq. 48 gives only near-zero values. Note, that units are not critical for the evaluation of the derived equations. Therefore, arbitrary units (a.u) are used. Also note that only values on the x and y axes on an individual panel should be compared. Value on different panels should not be compared.

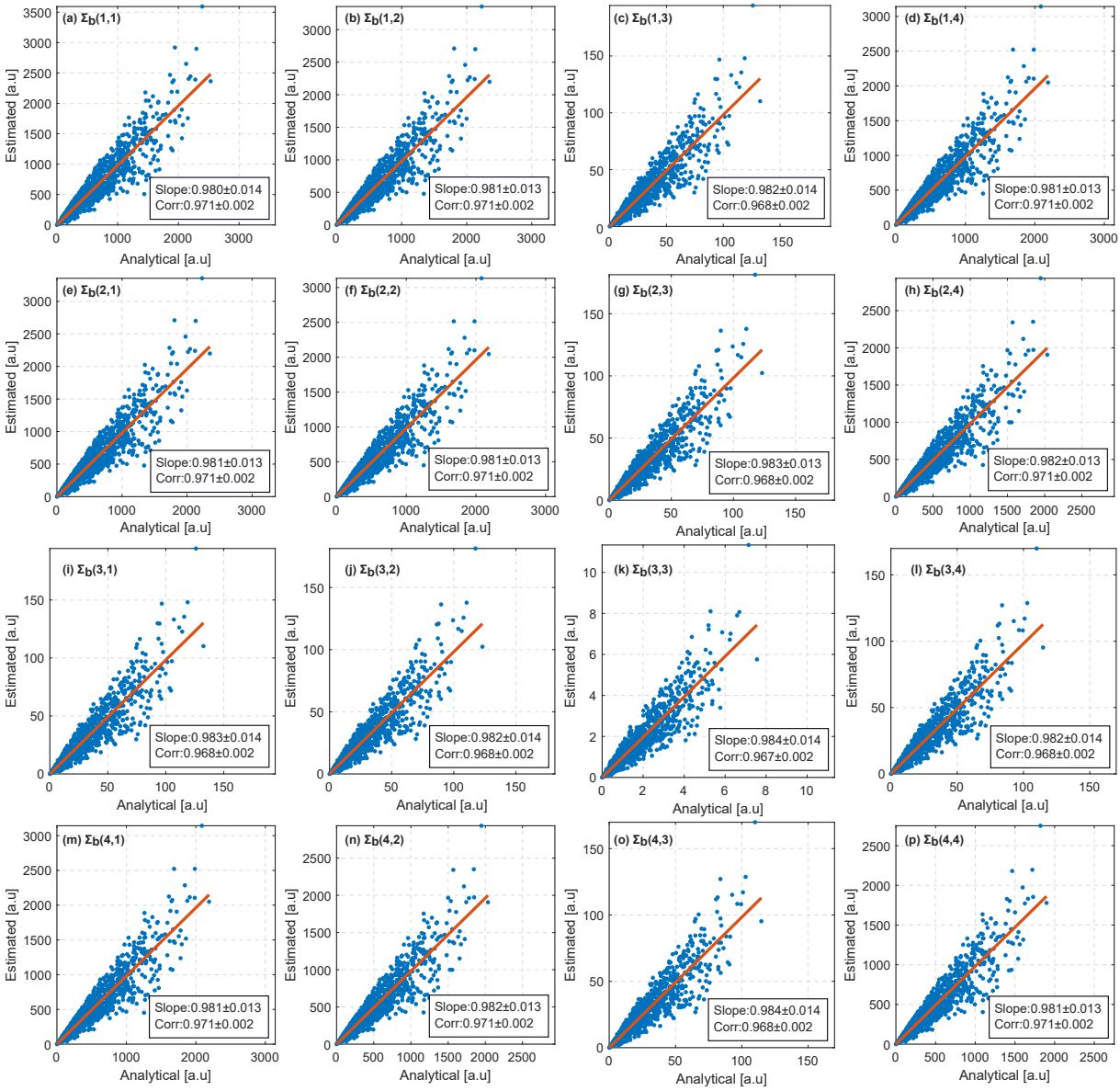

Figure 6. Comparison of $\hat{\Sigma}_b$ estimated from the radar measurements with Σ_b obtained from Eq. 46. Elements of Σ_b are given on the x-axes. Elements of $\hat{\Sigma}_b$ are given on the y-axes. The first and the second numbers in brackets indicate the row and the column of the corresponding matrix, respectively. Linear regressions are shown by red lines. Slopes of the linear regressions and Pearson correlations are given in boxes in each panel. Uncertainties in the slope and the correlation are represented by $\pm$ one standard deviation of the corresponding parameter. The standard deviations are obtained using the bootstrapping. Note, that units are not critical for the evaluation of the derived equations. Therefore, arbitrary units (a.u) are used.

5.5 Evaluation of $\boldsymbol{\Sigma_b}$

Figure 6 shows a comparison of elements of error covariance matrices $\hat{\Sigma}_b$ estimated from the radar measurements with those calculated using Eq. 46. Estimated and calculated elements are in a good agreement. Linear regressions shown in the panels by red lines have slopes close to 1. Pearson correlations between estimated and calculated elements exceed 0.96. These results indicate an agreement of the theoretical calculation with measurements and, thus, confirm correctness of Eq. 46. It is, thus, concluded that any application of spectral polarimetric measurements which require the estimate of the error covariance matrix (e.g. variational retrievals, data assimilation, and sensitivity analysis) should be performed in the space of observations $\hat{\boldsymbol{b}}$ rather than $\hat{\boldsymbol{c}}$.

6 Summary and outlook

Spectral and polarimetric cloud radar observations have a great potential in the cloud science (Kollias et al., 2020). Decades of such measurements have been already collected by e.g. the ARM (Atmospheric Radiation Measurement) and CLOUDNET communities. An advanced application of these vast datasets requires an accurate characterization of measurement uncertainties. Systematic errors in moment radar data and polarimetric variables have been discussed in many studies. Random measurement errors, in contrast, are rarely considered in literature. The are three main problems in existing random-error-characterization methods, namely (1) a lack of joint PDF for averaged polarimetric measurements, (2) neglection of non-diagonal components of the error covariance matrix, and (3) inaccuracy of the first-order approximation in variances of polarimetric variables. This study, thus, aims to provide solutions for these three problems.

Equations provided in Sec. 3 give an exact mathematical solution for the joint PDFs of spectral polarimetric observations. The PDFs are given for two equivalent representations of the measurements: (1) $\boldsymbol{b} = (B_{hh}, R_{hv}, J_{hv}, B_{vv})^{\mathrm{T}}$, and (2) $\boldsymbol{c} = (B_{hh}, Z_{DR}, \rho_{HV}, \Phi_{DP})^{\mathrm{T}}$. The obtained equations take into account non-coherent averaging of spectra, which is applied by a majority of cloud radars to improve the sensitivity. Maximum likelihood estimators of $\boldsymbol{b}$ based on Eqs. 36 and 39 were compared with the estimator based on longer averaging. The comparison was based on dual-polarimetric cloud radar observations. The comparison showed a good agreement. Both PDFs can be equivalently used for methods based on the maximum likelihood and Bayesian inference.

Section 4 is focused on the error covarince matrix required for a number of applications such as data assimilation, sensitivity analysis, and variational retrievals. The error covariance matrices Σ_b and Σ_c for $\boldsymbol{b}$ and $\boldsymbol{c}$, respectively, are obtained using the characteristic functions of the PDFs described in Sec. 3. Since the calculation of the $\boldsymbol{c}$ includes highly non-linear functions, Σ_c was derived using the first-order Taylor approximation. The same approach was used by Bringi and Chandrasekar (2001) to get equations for variances of polarimetric observations.

The error covariance matrices were evaluated using I/Q observations from a polarimetric W-band radar. It is illustrated that elements of Σ_c have considerable differences from those estimated from the measurements. First, we found differences in variances of Z_{DR}, ρ_{HV}, Φ_{DP} of up to factor of 10, 5, and 100, respectively. Second, the calculated variance of Φ_{DP} shows unrealistically high values by far exceeding the range of possible values. Third, most of the off-diagonal terms of Σ_c

are not correlated with corresponding values estimated from observations. We relate the differences to the first-order Taylor approximation. The Taylor approximation assumes linear relations between elements of the vector $\boldsymbol{b}$ and the elements of the vector $\boldsymbol{c}$, while the relations include highly non-linear functions. In contrast, Σ_b agrees well with the observations. The correlation between calculated elements of Σ_b with those estimated from the observations exceeds 0.965.

Thus, based on the results found within this study, it is recommended to use the vector $\boldsymbol{b}$ to represent polarimetric cloud radar observations for applications requiring the error covariance matrix. This representation has a better characterization of random errors in comparison with widely used representation $\boldsymbol{c}$. When the signal to noise ratio is high (> 35 dB), however, the variances are quite low and the Taylor approximation may give reasonable results.

In order to demonstrate a practical application of the developed characterization of the measurements errors, a few retrieval techniques are being currently developed. The first one is an improvement of the ice-share retrieval described in Myagkov et al. (2016a). Another one is an adoption of the drop-size-distribution from Tridon and Battaglia (2015) for dual-polarimeteric cloud radar observations.

Code and data availability. I/Q data used in this study are available on Zenodo (Myagkov and Unal, 2021, https://doi.org/10.5281/zenodo.5126813). MATLAB code used to process I/Q data is provided in the supplement to this paper. Ready-to-use MATLAB implementations for Eqs. 36, 39, 46, and 48 are given in the supplement.

Appendix A: Diagonalization matrix Q

The operator $\mathbf{Q}$, which is used to diagonalize the covariance matrix $\mathbf{B}$ in Eq. 20, is calculated as follows (Kanareykin et al., 1968, chapter 2.5):

$$\mathbf{Q} = \begin{pmatrix} q_{11} & \dot{q}_{12} \\ -\dot{q}_{12}^{*} & q_{11} \end{pmatrix}, \tag{A1}$$

where

$$q_{11} = \left(1 + \left|\dot{d}\right|^2\right)^{-0.5}, \tag{A2}$$

$$\dot{q}_{12} = -\dot{d}^{*} q_{11}, \tag{A3}$$

$$d = \frac{\dot{B}_{hv}^{*}}{0.5\left[\mathrm{Tr}\mathbf{B} + \sqrt{\mathrm{Tr}\mathbf{B}^2 - 4\det(\mathbf{B})}\right] - B_{vv}}. \tag{A4}$$

In Eq. A4 Tr is the matrix trace.

Appendix B: Derivation of likelihood functions

B1 Change of variables in a PDF

Consider a vector $\boldsymbol{a}$ with n random variables $a_{1\ldots n}$. Assume the joint PDF $f_a(\boldsymbol{a})$ of the variables is known. The joint PDF $f_y(\boldsymbol{y})$ of a vector

$$\boldsymbol{y} = G(\boldsymbol{a}) \tag{B1}$$

can be found changing the variables in $f_a(\boldsymbol{a})$:

$$f_y(\boldsymbol{y}) = |\mathbf{J}| f_a\left[G^{-1}(\boldsymbol{y})\right], \tag{B2}$$

where G^{-1} is reverse transformation from $\boldsymbol{y}$ to $\boldsymbol{a}$ and $\mathbf{J}$ is the determinant of the Jacobian of the transformation $\boldsymbol{a} = G^{-1}(\boldsymbol{y})$.

B2 Likelihood functions for D_{cc} and D_{xx}

It is known, that the PDF of z_s being a sum of squares of independent standard normal samples (i.e. distributed normally with 0 mean and standard deviation of 1) is the chi-squared distribution $\chi^2_k(z_s)$, where the degree of freedom k shows how many samples have been summed. Taking into account that:

$$\hat{D}_{cc} = N_s^{-1}\sigma_c^2\left\{\sigma_c^{-2}\sum_{l=1}^{N_s}\mathrm{Re}\left(\dot{S}_c\right)_l^2 + \sigma_c^{-2}\sum_{l=1}^{N_s}\mathrm{Im}\left(\dot{S}_c\right)_l^2\right\}, \tag{B3}$$

where the first and the second summed terms in the curly brackets are sums of squares of independent standard normal samples, the likelihood function $f\left(\hat{D}_{cc}|\sigma_c, N_s\right)$ can be found by changing the variable z_s to $N_s\sigma_c^{-2}\hat{D}_c$:

$$f\left(\hat{D}_{cc}|\sigma_c, N_s\right) = \frac{N_s}{\sigma_c^2}\chi^2_{2N_s}\left(\frac{N_s}{\sigma_c^2}\hat{D}_{cc}\right). \tag{B4}$$

The factor of 2 in the degree of freedom is because there are $2N_s$ summed components in the curly brackets in Eq. B3. The equation for $\hat{D}_{xx}$ is derived in a similar manner as for $\hat{D}_{cc}$ resulting in:

$$f\left(\hat{D}_{xx}|\sigma_x, N_s\right) = \frac{N_s}{\sigma_x^2}\chi^2_{2N_s}\left(\frac{N_s}{\sigma_x^2}\hat{D}_{xx}\right). \tag{B5}$$

B3 Likelihood functions for R_{cx} and J_{cx}

Nadarajah and Pogány (2016) provide a solution for the PDF of an averaged multiplication z_m of two standard normal variables. For two uncorrelated variables the PDF is defined as follows:

$$f_z(z_m) = \frac{n^{(n+1)/2}2^{(1-n)/2}|z_m|^{(n-1)/2}}{\sqrt{\pi}\Gamma(n/2)}K_{(1-n)/2}\left(n|z_m|\right), \tag{B6}$$

where n is the number of averaged multiplications, Γ is the gamma function, and K_μ is the Bessel function of the second kind of order μ.

$\hat{R}_{cx}$ is calculated as follows:

$$\hat{R}_{cx} = 2\sigma_c\sigma_x \left\{ \frac{1}{2N_s\sigma_c\sigma_x} \left[\sum_{l=1}^{N_s} \mathrm{Re}\left(\dot{S}_c\right) \mathrm{Re}\left(\dot{S}_x\right) + \sum_{l=1}^{N_s} \mathrm{Im}\left(\dot{S}_c\right) \mathrm{Im}\left(\dot{S}_x\right) \right] \right\}, \tag{B7}$$

where the term in the curly brackets is an average over $2N_s$ multiplications of independent standard normal samples. In this case, the likelihood function $f\left(\hat{R}_{cx}|\sigma_c, \sigma_x, N_s\right)$ can be found by changing z_m by $(2\sigma_c\sigma_x)^{-1}\hat{R}_{cx}$:

$$f\left(\hat{R}_{cx}|\sigma_c, \sigma_x, N_s\right) = \frac{(2N_s)^a |\hat{R}_{cx}|^{-b}}{\sqrt{\pi} 2^{2N_s} (\sigma_c\sigma_x)^a \Gamma(N_s)} K_b\left(\frac{N_s|\hat{R}_{cx}|}{\sigma_c\sigma_x}\right), \tag{B8}$$

where $a = (2N_s + 1)/2$, $b = (1 - 2N_s)/2$, Γ is the gamma function, and K_μ is the Bessel function of the second kind of order μ. When $\hat{R}_{cx} \to 0$, the modified Bessel function $K_b\left(N_s|\hat{R}_{cx}|(\sigma_c\sigma_x)^{-1}\right) \to \infty$. Therefore, for $\hat{R}_{cx}$ close to 0, the following approximation based on Eqs. 9.6.6 and 9.6.8 from Abramowitz and Stegun (1972) should be used:

$$f\left(\hat{R}_{cx}|\sigma_c, \sigma_x, N_s\right) \approx \frac{N_s\Gamma(-b)}{2\sqrt{\pi}\sigma_c\sigma_x\Gamma(N_s)}. \tag{B9}$$

Formulas for $\hat{J}_{cx}$ are defined in a similar manner:

$$f\left(\hat{J}_{cx}|\sigma_c, \sigma_x, N_s\right) = \frac{(2N_s)^a |\hat{J}_{cx}|^{-b}}{\sqrt{\pi} 2^{2N_s} (\sigma_c\sigma_x)^a \Gamma(N_s)} K_b\left(\frac{N_s|\hat{J}_{cx}|}{\sigma_c\sigma_x}\right), \tag{B10}$$

with the approximation for $\hat{J}_{cx}$ close to 0:

$$f\left(\hat{J}_{cx}|\sigma_c, \sigma_x, N_s\right) \approx \frac{N_s\Gamma(-b)}{2\sqrt{\pi}\sigma_c\sigma_x\Gamma(N_s)}. \tag{B11}$$

B4 Monte Carlo evaluation of Eqs. B4, B5, B8, and B10

For the equation evaluation a simulated dataset was generated. In total 1000 sets of distributions were simulated using the Monte Carlo approach. A single set included distributions of $\hat{B}_{cc}$, $\hat{B}_{xx}$, $\hat{R}_{cx}$, and $\hat{J}_{cx}$. For a single set 10^5 vectors $\hat{\boldsymbol{b}}$ were generated. A single vector $\hat{\boldsymbol{b}}$ resulted from N_s randomly generated vectors $\boldsymbol{m}$. For a single set of distributions a single covariance matrix $\mathbf{B}$ was taken. The elements of the covariance matrix $\mathbf{B}$ and N_s were randomly generated according to the following rules (values have linear arbitrary units):

1. B_{hh} is a sum of mean powers of signal P_{sh} and noise P_{nh}.
2. B_{vv} is a sum of mean powers of signal P_{sv} and noise P_{nv}.
3. $P_{nh} = P_{nv} = 1$
4. P_{sh} and P_{sv} were randomly and independently generated using the uniform distribution from 1 to 5.
5. $\dot{B}_{hv}$ was calculated as $\rho_{HV} e^{i\Phi_{DP}} \sqrt{P_{sh} P_{sv}}$.

Table B1. Percentage of test-statistic values exceeding critical values for different significance levels. Percentages are given in %. Names of 4 columns on the right side of the table indicate for which distribution a percentage is given.

Significance level	Critical value	$f\left(\hat{D}_{cc}\|\sigma_c, N_s\right)$	$f\left(\hat{R}_{cx}\|\sigma_c, N_s\right)$	$f\left(\hat{J}_{cx}\|\sigma_c, N_s\right)$	$f\left(\hat{D}_{xx}\|\sigma_c, N_s\right)$
0.95	16.919	6.9	5.2	5.8	5.9
0.975	19.023	3.8	3.4	2.7	2.9
0.99	21.666	1.0	1.3	1.0	1.2

6. ρ_{HV} was chosen randomly using the uniform distribution from 0 to 1.

7. Φ_{DP} was chosen randomly using the uniform distribution from 0 to 2π.

8. N_s was chosen as a random integer number in the range from 2 to 80.

From the covariance matrix $\mathbf{B}$ the true covariance matrix Σ_m was obtained. $10^5 \times N_s$ vectors $\boldsymbol{m}$ were generated according to the PDF given in Eq. 2. Then, 10^5 elements of the $\hat{\boldsymbol{b}}$ were calculated according to Eqs. 15–18. Elements of the vector $\hat{\boldsymbol{d}}$ were derived from the vectors $\hat{\boldsymbol{b}}$ using Eq. 27.

Using the 10^5 vectors $\hat{\boldsymbol{d}}$ individual histograms for each of the variables $\hat{B}_{cc}$, $\hat{B}_{xx}$, $\hat{R}_{cx}$, and $\hat{J}_{cx}$ are derived. A histogram has 10 bins covering the range from the minimum to maximum values of the corresponding variable. Widths of bins were adjusted to have 10000 samples in each bin. For the same bins the expected number of samples is calculated using the corresponding PDF. Since integration of Eqs. B4, B5, B8, and B10 is challenging, the integration is done numerically. Then the Pearson's chi-squared test is applied. The same procedure is repeated for all 1000 sets of distributions. Thus, for each PDF (Eqs. B4, B5, B8, and B10) 1000 test-statistic values were obtained.

The Pearson's chi-squared test implies a comparison of the test-statistic values with a critical values for a given level of significance. A test-statistic value exceeding the critical value would indicate that there is a chance (equal to the significance level) that the data significantly differs from the PDF. There is, however, a small chance that the conclusion that the data differs from the PDF is erroneous. Table B1 shows the percentage of the test-statistic values exceeding critical values. It can be seen that the amount of test-statistic values exceeding corresponding critical values is very close to the theoretical values, i.e. 5, 2.5, and 1 % at 0.95, 0.975, and 0.99 significance levels, respectively. This confirms the validity of the obtained PDFs.

B5 Jacobian $\mathbf{J}_{bd}$ of the transformation from $\hat{b}$ to $\hat{d}$

Using Eqs. 21–22 $\mathbf{J}_{bd}$ can be written as follows:

$$\mathbf{J}_{bd} = \begin{vmatrix} \frac{\partial D_{cc}}{\partial B_{hh}} & \frac{\partial D_{cc}}{\partial R_{hv}} & \frac{\partial D_{cc}}{\partial J_{hv}} & \frac{\partial D_{cc}}{\partial B_{vv}} \\ \frac{\partial R_{cx}}{\partial B_{hh}} & \frac{\partial R_{cx}}{\partial R_{hv}} & \frac{\partial R_{cx}}{\partial J_{hv}} & \frac{\partial R_{cx}}{\partial B_{vv}} \\ \frac{\partial J_{cx}}{\partial B_{hh}} & \frac{\partial J_{cx}}{\partial R_{hv}} & \frac{\partial J_{cx}}{\partial J_{hv}} & \frac{\partial J_{cx}}{\partial B_{vv}} \\ \frac{\partial D_{xx}}{\partial B_{hh}} & \frac{\partial D_{xx}}{\partial R_{hv}} & \frac{\partial D_{xx}}{\partial J_{hv}} & \frac{\partial D_{xx}}{\partial B_{vv}} \end{vmatrix} =$$

$$\begin{vmatrix} q_{11}^2 & |\dot{q}_{12}|^2 & -2q_{11}R_{12} & -2q_{11}J_{12} \\ |\dot{q}_{12}|^2 & q_{11}^2 & 2q_{11}R_{12} & 2q_{11}J_{12} \\ q_{11}R_{12} & -q_{11}R_{12} & q_{11}^2 - R_{12}^2 + J_{12}^2 & -2R_{12}J_{12} \\ q_{11}J_{12} & -q_{11}J_{12} & -2R_{12}J_{12} & q_{11}^2 + R_{12}^2 - J_{12}^2 \end{vmatrix} = (q_{11}^2 + |q_{12}|^2)^4. \quad \text{(B12)}$$

Taking into account Eqs. A2 and A3, $\mathbf{J}_{bd} = 1$.

B6 Jacobian $\mathbf{J}_{cb}$ of the transformation from $\hat{c}$ to $\hat{b}$

Using Eqs. 21–22 $\mathbf{J}_{cb}$ can be written as follows:

$$\mathbf{J}_{cb} = \begin{vmatrix} \frac{\partial B_{hh}}{\partial B_{hh}} & \frac{\partial B_{hh}}{\partial Z_{DR}} & \frac{\partial B_{hh}}{\partial \rho_{HV}} & \frac{\partial B_{hh}}{\partial \Phi_{DP}} \\ \frac{\partial R_{hv}}{\partial B_{hh}} & \frac{\partial R_{hv}}{\partial Z_{DR}} & \frac{\partial R_{hv}}{\partial \rho_{HV}} & \frac{\partial R_{hv}}{\partial \Phi_{DP}} \\ \frac{\partial J_{hv}}{\partial B_{hh}} & \frac{\partial J_{hv}}{\partial Z_{DR}} & \frac{\partial J_{hv}}{\partial \rho_{HV}} & \frac{\partial J_{hv}}{\partial \Phi_{DP}} \\ \frac{\partial B_{vv}}{\partial B_{hh}} & \frac{\partial B_{vv}}{\partial R_{hv}} & \frac{\partial B_{vv}}{\partial J_{hv}} & \frac{\partial B_{vv}}{\partial B_{vv}} \end{vmatrix} =$$

$$\begin{vmatrix} 1 & 0 & 0 & 0 \\ \rho_{HV}\cos(\Phi_{DP})Z_{DR}^{-0.5} & -0.5B_{hh}\rho_{HV}\cos(\Phi_{DP})Z_{DR}^{-1.5} & B_{hh}\cos(\Phi_{DP})Z_{DR}^{-0.5} & -B_{hh}\rho_{HV}\sin(\Phi_{DP})Z_{DR}^{-0.5} \\ \rho_{HV}\sin(\Phi_{DP})Z_{DR}^{-0.5} & -0.5B_{hh}\rho_{HV}\sin(\Phi_{DP})Z_{DR}^{-1.5} & B_{hh}\sin(\Phi_{DP})Z_{DR}^{-0.5} & -B_{hh}\rho_{HV}\cos(\Phi_{DP})Z_{DR}^{-0.5} \\ Z_{DR}^{-1} & -B_{hh}Z_{DR}^{-2} & 0 & 0 \end{vmatrix} =$$

$$-B_{hh}^3 Z_{DR}^{-3}\rho_{HV} \quad \text{(B13)}$$

Appendix C: Variances of elements of the vector $\hat{d}$

To derive solutions for mean and variances of elements of $\hat{\boldsymbol{d}}$, the distribution of the elements is represented by characteristic functions. A γ-th raw statistical moment M_γ of a random variable with a characteristic function $\phi(t)$ can be found as follows:

$$M_\gamma = i^{-\gamma} \frac{d^\gamma \phi(t)}{dt^\gamma}\Big|_{t=0}, \tag{C1}$$

The calculation of derivatives of the characteristic functions is in general easier to obtain than integration of the corresponding PDFs.

The characteristic function of the chi-squared distribution $\chi^2_k(z_s)$ is

$$\phi_s(t) = (1-2it)^{-k/2}. \tag{C2}$$

Therefore, the characteristic function for $\hat{D}_{cc}$ for a given σ_c and N_s can be written in the following way:

$$\phi_{cc}(t) = \left(1 - \frac{2i\sigma_c^2 t}{N_s}\right)^{-N_s} \tag{C3}$$

The mean value and variance of $\hat{D}_{cc}$ are calculated as follows:

$$\overline{\hat{D}_{cc}} = \frac{1}{i}\frac{d\phi_{cc}(t)}{dt}\Big|_{t=0} = 2\sigma_c^2, \tag{C4}$$

$$\mathrm{var}(\hat{D}_{cc}) = -\frac{d^2\phi_{cc}(t)}{dt^2}\Big|_{t=0} - \overline{\hat{D}_{cc}}^2 = \frac{4\sigma_c^4}{N_s}. \tag{C5}$$

Similarly,

$$\overline{\hat{D}_{xx}} = \frac{1}{i}\frac{d\phi_{xx}(t)}{dt}\Big|_{t=0} = 2\sigma_x^2, \tag{C6}$$

$$\mathrm{var}(\hat{D}_{xx}) = \frac{4\sigma_x^4}{N_s}. \tag{C7}$$

Based on Nadarajah and Pogány (2016) the characteristic function corresponding to $f_z(z_m)$ is

$$\phi_z(t) = \left(1 + \frac{t^2}{n^2}\right)^{-n/2}. \tag{C8}$$

Therefore, the characteristic function for $\hat{R}_{cx}$ and $\hat{J}_{cx}$ for given σ_c, σ_x, and N_s is as follows:

$$\phi_{cx}(t) = \left(1 + \frac{\sigma_c^2\sigma_x^2 t^2}{N_s^2}\right)^{-N_s/2}. \tag{C9}$$

As expected for a multiplication of two uncorrelated variables, the mean values of $\hat{R}_{cx}$ and $\hat{J}_{cx}$

$$\overline{\hat{R}_{cx}} = \overline{\hat{J}_{cx}} = \frac{1}{i}\frac{d\phi_{cx}(t)}{dt}\Big|_{t=0} = 0. \tag{C10}$$

The variance of $\hat{R}_{cx}$ and $\hat{J}_{cx}$ can be found as follows:

$$\mathrm{var}(\hat{R}_{cx}) = \mathrm{var}(\hat{J}_{cx}) = -\frac{d^2\phi_{cx}(t)}{dt^2}\Big|_{t=0} = \frac{\sigma_c^2\sigma_x^2}{2N_s}. \tag{C11}$$

Table D1. Main symbols used throughout the study. The overdot indicates a complex number. Indices h and v indicate the polarization of the receiver channel. The overhat indicates a measured quantity.

Symbol	Description
Γ	Gamma function
ρ_{HV} and $\hat{\rho}_{HV}$	Correlation coefficient for a spectral line
Φ_{DP} and $\hat{\Phi}_{DP}$	Differential phase for a spectral line
σ_h	Standard deviation of $\hat{R}_h$ and $\hat{J}_h$
σ_v	Standard deviation of $\hat{R}_v$ and $\hat{J}_v$
σ_c	Standard deviation of $\hat{R}_c$ and $\hat{J}_c$
σ_x	Standard deviation of $\hat{R}_x$ and $\hat{J}_x$
Σ_m	Error covariance matrix of $\hat{\boldsymbol{m}}$
Σ_d	Error covariance matrix of $\hat{\boldsymbol{d}}$
Σ_b and $\hat{\Sigma}_b$	Error covariance matrix of $\hat{\boldsymbol{b}}$
Σ_c and $\hat{\Sigma}_c$	Error covariance matrix of $\hat{\boldsymbol{c}}$
$\phi(t)$	characteristic function
$\phi_s(t)$	characteristic function for z_s
$\phi_{cc}(t)$	characteristic function for $\hat{D}_{cc}$
$\phi_{cx}(t)$	characteristic function for $\hat{R}_{cx}$ and $\hat{J}_{cx}$
$\phi_z(t)$	characteristic function for z_m
χ^2_k	chi-squared distribution with k degrees of freedom
$*$	Complex conjugation sign
$\dagger$	Hermitian conjugate sign
$\boldsymbol{b}$	the column vector elements of which are B_{hh}, R_{hv}, J_{hv}, and B_{vv}
$\hat{\boldsymbol{b}}$	the column vector elements of which are $\hat{B}_{hh}$, $\hat{R}_{hv}$, $\hat{J}_{hv}$, and $\hat{B}_{vv}$
$\mathbf{B}$ and $\hat{\mathbf{B}}$	2×2 covariance matrix describing polarimetric measurements in a single spectral line in the $h - v$ basis
B_{hh}, $\dot{B}_{hv}$, and B_{vv}	elements of the covariance matrix $\mathbf{B}$
$\hat{B}_{hh}$ and $\hat{B}_{vv}$	diagonal elements of the covariance matrix $\hat{\mathbf{B}}$
$\boldsymbol{c}$	the column vector elements of which are B_{hh}, Z_{DR}, ρ_{HV}, and Φ_{DP}
$\hat{\boldsymbol{c}}$	the column vector elements of which are $\hat{B}_{hh}$, $\hat{Z}_{DR}$, $\hat{\rho}_{HV}$, and $\hat{\Phi}_{DP}$

Table D2. Continue of Table D1.

Symbol	Description
$\hat{\boldsymbol{d}}$	Column vector elements of which are $\hat{D}_{cc}$, $\hat{R}_{cx}$, $\hat{J}_{cx}$, and $\hat{D}_{xx}$
D_{cc} and D_{xx}	Diagonal elements of the covariance matrix $\mathbf{D}$
$\hat{D}_{cc}$,$\hat{D}_{vv}$, and $\hat{D}_{cx}$	Elements of the covariance matrix $\hat{\mathbf{D}}$
$\mathbf{D}$ and $\hat{\mathbf{D}}$	2×2 covariance matrix describing polarimetric measurements in a single spectral line in the $c - x$ basis
$\boldsymbol{e}$	measurement column vector in the $h - v$ basis
$\boldsymbol{e}_D$	measurement column vector in the $c - x$ basis
$f(\hat{D}_{cc}\|\boldsymbol{b}, N_s)$	PDF of $\hat{D}_{cc}$ for a given $\boldsymbol{b}$ and N_s
$f(\hat{R}_{cx}\|\boldsymbol{b}, N_s)$	PDF of $\hat{R}_{cx}$ for a given $\boldsymbol{b}$ and N_s
$f(\hat{J}_{cx}\|\boldsymbol{b}, N_s)$	PDF of $\hat{J}_{cx}$ for a given $\boldsymbol{b}$ and N_s
$f(\hat{D}_{xx}\|\boldsymbol{b}, N_s)$	PDF of $\hat{D}_{xx}$ for a given $\boldsymbol{b}$ and N_s
$f_m(\hat{\boldsymbol{m}}\|\Sigma_m)$	joint PDF of $\hat{\boldsymbol{m}}$ for a given Σ_m
$f_d(\hat{\boldsymbol{d}}\|\boldsymbol{b}, N_s)$	joint PDF of $\hat{\boldsymbol{d}}$ for a given $\boldsymbol{b}$ and N_s
$f_b(\hat{\boldsymbol{b}}\|\boldsymbol{b}, N_s)$	joint PDF of $\hat{\boldsymbol{b}}$ for a given $\boldsymbol{b}$ and N_s
$f_c(\hat{\boldsymbol{c}}\|\boldsymbol{b}, N_s)$	joint PDF of $\hat{\boldsymbol{c}}$ for a given $\boldsymbol{b}$ and N_s
i	Imaginary unit
$I_{h,v}$	Measured in-phase component measured by the radar receiver in a range bin
J_{12}	Imaginary part of $\dot{q}_{12}$
$\hat{J}_{cx}$	Imaginary part of $\hat{D}_{cx}$
$\hat{J}_h$ and $\hat{J}_v$	Imaginary parts of $\dot{S}_h$ and $\dot{S}_v$, respectively
J_{hv}	Imaginary part of $\dot{B}_{hv}$
$\hat{J}_{hv}$	Imaginary part of the covariance between $\dot{S}_h$ and $\dot{S}_v$
$\mathbf{J}_{bd}$	Jacobian of the transformation from $\hat{\boldsymbol{b}}$ to $\hat{\boldsymbol{d}}$
$\mathbf{J}_{cb}$	Jacobian of the transformation from $\hat{\boldsymbol{c}}$ to $\hat{\boldsymbol{b}}$
K_μ	Bessel function of the second kind of order μ
$\hat{\boldsymbol{m}}$	Measurement vector, which elements are real and imaginary parts of $\dot{S}_h$ and $\dot{S}_v$
M_γ	γ-th raw statistical moment of a random variable
N_s	Number of spectra used for averaging
N_{fft}	Number of pulses/chirps used to calculate the Doppler spectra
$Q_{h.v}$	Measured quadrature component measured by the radar receiver in a range bin

Table D3. Continue of Table D1.

Symbol	Description
$\mathbf{Q}$	Matrix used to diagonalize the matrix $\mathbf{B}$
q_{11}, $\dot{q}_{12}$, and q_{22}	Elements of the matrix $\mathbf{Q}$
q	correlation between $\hat{R}_h$ and $\hat{R}_v$
s	correlation between $\hat{R}_h$ and $\hat{J}_v$
R_{12}	real part of $\dot{q}_{12}$
$\hat{R}_h$ and $\hat{R}_v$	real parts of $\dot{S}_h$ and $\dot{S}_v$, respectively
R_{hv}	real part of $\dot{B}_{hv}$
$\hat{R}_{hv}$	Real part of the covariance between $\dot{S}_h$ and $\dot{S}_v$
$\hat{R}_{cx}$	Real part of $\hat{D}_{cx}$
$\dot{S}_{h,v}$	Measured complex amplitude for a spectral line
$\mathbf{S}$	the 4×4 sensitivity matrix
T	the transposition sign
t	argument of a characteristic function
VAR_{bhh}	Variance of $\hat{B}_{hh}$ approximated from Bringi and Chandrasekar (2001)
VAR_{zdr}	Variance of $\hat{Z}_{DR}$ approximated from Bringi and Chandrasekar (2001)
VAR_{ρ}	Variance of $\hat{\rho}_{HV}$ approximated from Bringi and Chandrasekar (2001)
VAR_{Φ}	Variance of $\hat{\Phi}_{DP}$ approximated from Bringi and Chandrasekar (2001)
Z_{DR} and $\hat{Z}_{DR}$	Differential reflectivity for a spectral line
z_s	a sum of squares of independent standard normal samples
z_m	averaged multiplication of two standard normal variables

Appendix D: Table of symbols

Author contributions. AM derived equations for PDFs and error covariance matrices, made evaluation using the radar observations, and prepared the first draft of the manuscript. DO reviewed the draft and essentially improved the manuscript.

Competing interests. AM is an employee of Radiometer Physics GmbH. DO declares no competing interests.

Acknowledgements. This work was carried out as a collaboration within the IMPRINT (Understanding Ice Microphysical Processes by combining multi-frequency and spectral Radar polarImetry aNd super-parTicle modelling, Project Number 408011764) project, which is a part of the German Research Foundation (DFG) Priority Program SPP2115 PROM (Fusion of Radar Polarimetry and Numerical Atmospheric Modelling Towards an Improved Understanding of Cloud and Precipitation Processes). The authors acknowledge Ruisdael Observatory, the Netherlands and Christine Unal from TU Delft for granting an access to the W-band radar in Cabauw to collect I/Q data used in this study. Work of DO is funded by the German Research Foundation (DFG) under the grant SCHE 2074/1-1 (SPP HALO).

References

Abramowitz, M. and Stegun, I. A.: Handbook of Mathematical Functions With Formulas, Graphs, and Mathematical Tables, United States National Bureau of Standards, 10th edn., 1972.

Acquistapace, C., Kneifel, S., Löhnert, U., Kollias, P., Maahn, M., and Bauer-Pfundstein, M.: Optimizing observations of drizzle onset with millimeter-wavelength radars, Atmospheric Measurement Techniques, 10, 1783–1802, https://doi.org/10.5194/amt-10-1783-2017, 2017.

Borque, P., Luke, E., and Kollias, P.: On the unified estimation of turbulence eddy dissipation rate using Doppler cloud radars and lidars, Journal of Geophysical Research: Atmospheres, 121, 5972–5989, https://doi.org/https://doi.org/10.1002/2015JD024543, 2016.

Bringi, V. N. and Chandrasekar, V.: Polarimetric Doppler Weather Radar, Cambridge University Press, 2001.

Bühl, J., Seifert, P., Engelmann, R., and Ansmann, A.: Impact of vertical air motions on ice formation rate in mixed-phase cloud layers, 2, https://doi.org/10.1038/s41612-019-0092-6.

Bühl, J., Ansmann, A., Seifert, P., Baars, H., and Engelmann, R.: Toward a quantitative characterization of heterogeneous ice formation with lidar/radar: Comparison of CALIPSO/CloudSat with ground-based observations, Geophysical Research Letters, 40, 4404–4408, https://doi.org/10.1002/grl.50792, 2013.

Bühl, J., Seifert, P., Radenz, M., Baars, H., and Ansmann, A.: Ice crystal number concentration from lidar, cloud radar and radar wind profiler measurements, Atmospheric Measurement Techniques, 12, 6601–6617, https://doi.org/10.5194/amt-12-6601-2019, 2019.

Cao, Q., Zhang, G., and Xue, M.: A Variational Approach for Retrieving Raindrop Size Distribution from Polarimetric Radar Measurements in the Presence of Attenuation, Journal of Applied Meteorology and Climatology, 52, 169–185, https://doi.org/10.1175/JAMC-D-12-0101.1, 2013.

Chandrasekar, V., Baldini, L., Bharadwaj, N., and Smith, P. L.: Calibration procedures for global precipitation-measurement ground-validation radars, URSI Radio Science Bulletin, 2015, 45–73, https://doi.org/10.23919/URSIRSB.2015.7909473, 2015.

Chang, W.-Y., Vivekanandan, J., Ikeda, K., and Lin, P.-L.: Quantitative Precipitation Estimation of the Epic 2013 Colorado Flood Event: Polarization Radar-Based Variational Scheme, Journal of Applied Meteorology and Climatology, 55, 1477–1495, https://doi.org/10.1175/JAMC-D-15-0222.1, 2016.

Doviak, R. J., Zrnic, D. S., and Sirmans, D. S.: Doppler weather radar, Proceedings of the IEEE, 67, 1522–1553, https://doi.org/10.1109/PROC.1979.11511, 1979.

Dufournet, Y. and Russchenberg, H. W. J.: Towards the improvement of cloud microphysical retrievals using simultaneous Doppler and polarimetric radar measurements, Atmospheric Measurement Techniques, 4, 2163–2178, https://doi.org/10.5194/amt-4-2163-2011, 2011.

Görsdorf, U., Lehmann, V., Bauer-Pfundstein, M., Peters, G., Vavriv, D., Vinogradov, V., and Volkov, V.: A 35-GHz polarimetric Doppler radar for long term observations of cloud parameters - Description of system and data processing, Journal of Atmospheric and Oceanic Technology, 32, 675–690, https://doi.org/10.1175/JTECH-D-14-00066.1, 2015.

Hildebrand, P. H. and Sekhon, R. S.: Objective determination of the noise level in Doppler spectra, Journal of Applied Meteorology, 13, 808–811, https://doi.org/10.1175/1520-0450(1974)013<0808:ODOTNL>2.0.CO;2, 1974.

Hogan, R. J.: A Variational Scheme for Retrieving Rainfall Rate and Hail Reflectivity Fraction from Polarization Radar, Journal of Applied Meteorology and Climatology, 46, 1544, https://doi.org/10.1175/JAM2550.1, 2007.

Huang, H., Zhao, K., Zhang, G., Hu, D., and Yang, Z.: Optimized raindrop size distribution retrieval and quantitative rainfall estimation from polarimetric radar, Journal of Hydrology, 580, 124248, https://doi.org/10.1016/j.jhydrol.2019.124248, 2020.

Illingworth, A. J., Hogan, R. J., O'Connor, E. J., Bouniol, D., DelanoÃ«, J., Pelon, J., Protat, A., Brooks, M. E., Gaussiat, N., Wilson, D. R., Donovan, D. P., Baltink, H. K., van Zadelhoff, G.-J., Eastment, J. D., Goddard, J. W. F., Wrench, C. L., Haeffelin, M., Krasnov, O. A., Russchenberg, H. W. J., Piriou, J.-M., Vinit, F., Seifert, A., Tompkins, A. M., and WillÃ©n, U.: Cloudnet, Bulletin of the American Meteorological Society, 88, 883–898, https://doi.org/10.1175/BAMS-88-6-883, 2007.

Kalesse, H., Szyrmer, W., Kneifel, S., Kollias, P., and Luke, E.: Fingerprints of a riming event on cloud radar Doppler spectra: observations and modeling, Atmospheric Chemistry & Physics Discussions, 15, 28 619–28 658, https://doi.org/10.5194/acpd-15-28619-2015, 2015.

Kanareykin, D. B., Potechin, V. A., and Shishkin, I. F.: Marine Radio Polarimetry, Sudostroenie, [In Russian], 1968.

Kneifel, S. and Moisseev, D.: Long-Term Statistics of Riming in Nonconvective Clouds Derived from Ground-Based Doppler Cloud Radar Observations, Journal of Atmospheric Sciences, 77, 3495–3508, https://doi.org/10.1175/JAS-D-20-0007.1, 2020.

Kneifel, S., von Lerber, A., Tiira, J., Moisseev, D., Kollias, P., and Leinonen, J.: Observed relations between snowfall microphysics and triple-frequency radar measurements, Journal of Geophysical Research (Atmospheres), pp. 6034–6055, https://doi.org/10.1002/2015JD023156, 2015JD023156, 2015.

Kneifel, S., Kollias, P., Battaglia, A., Leinonen, J., Maahn, M., Kalesse, H., and Tridon, F.: First observations of triple-frequency radar Doppler spectra in snowfall: Interpretation and applications, Journal of Geophysical Research (Atmospheres), 43, 2225–2233, https://doi.org/10.1002/2015GL067618, 2016.

Kollias, P., Clothiaux, E. E., Miller, M. A., Albrecht, B. A., Stephens, G. L., and Ackerman, T. P.: Millimeter-Wavelength Radars: New Frontier in Atmospheric Cloud and Precipitation Research, Bulletin of the American Meteorological Society, 88, 1608–1624, https://doi.org/10.1175/BAMS-88-10-1608, 2007.

Kollias, P., Bharadwaj, N., Clothiaux, E. E., Lamer, K., Oue, M., Hardin, J., Isom, B., Lindenmaier, I., Matthews, A., Luke, E. P., Giangrande, S. E., Johnson, K., Collis, S., Comstock, J., and Mather, J. H.: The ARM Radar Network: At the Leading Edge of Cloud and Precipitation Observations, Bulletin of the American Meteorological Society, 101, E588–E607, https://doi.org/10.1175/BAMS-D-18-0288.1, 2020.

Küchler, N., Kneifel, S., Löhnert, U., Kollias, P., Czekala, H., and Rose, T.: A W-Band Radar-Radiometer System for Accurate and Continuous Monitoring of Clouds and Precipitation, Journal of Atmospheric and Oceanic Technology, 34, 2375–2392, https://doi.org/10.1175/JTECH-D-17-0019.1, 2017.

Kumjian, M.: Principles and Applications of Dual-Polarization Weather Radar. Part I: Description of the Polarimetric Radar Variables, Journal of Operational Meteorology, 1, 226–242, https://doi.org/10.15191/nwajom.2013.0119, 2013.

Lagarias, J. C., Reeds, J. A., Wright, M. H., and Wright, P. E.: Convergence Properties of the Nelder–Mead Simplex Method in Low Dimensions, SIAM Journal on Optimization, 9, 112–147, https://doi.org/10.1137/S1052623496303470, 1998.

Lee, J.-S., Hoppel, K. W., Mango, S. A., and Miller, A. R.: Intensity and phase statistics of multilook polarimetric and interferometric SAR imagery, IEEE Transactions on Geoscience and Remote Sensing, 32, 1017–1028, https://doi.org/10.1109/36.312890, 1994.

Lu, Y., Aydin, K., Clothiaux, E. E., and Verlinde, J.: Retrieving Cloud Ice Water Content Using Millimeter- and Centimeter-Wavelength Radar Polarimetric Observables, Journal of Applied Meteorology and Climatology, 54, 596–604, https://doi.org/10.1175/JAMC-D-14-0169.1, 2015.

Marple, S.: Digital Spectral Analysis: Second Edition, Dover Books on Electrical Engineering, Dover Publications, 2019.

Matrosov, S. Y.: Attenuation-Based Estimates of Rainfall Rates Aloft with Vertically Pointing Ka-Band Radars, Journal of Atmospheric and Oceanic Technology, 22, 43, https://doi.org/10.1175/JTECH-1677.1, 2005.

Matrosov, S. Y., Reinking, R. F., Kropfli, R. A., Martner, B. E., and Bartram, B. W.: On the Use of Radar Depolarization Ratios for Estimating Shapes of Ice Hydrometeors in Winter Clouds, Journal of Applied Meteorology, 40, 479–490, https://doi.org/10.1175/1520-0450(2001)040<0479:OTUORD>2.0.CO;2, 2001.

Matrosov, S. Y., May, P. T., and Shupe, M. D.: Rainfall Profiling Using Atmospheric Radiation Measurement Program Vertically Pointing 8-mm Wavelength Radars, Journal of Atmospheric and Oceanic Technology, 23, 1478, https://doi.org/10.1175/JTECH1957.1, 2006.

Matrosov, S. Y., Shupe, M. D., and Djalalova, I. V.: Snowfall Retrievals Using Millimeter-Wavelength Cloud Radars, Journal of Applied Meteorology and Climatology, 47, 769, https://doi.org/10.1175/2007JAMC1768.1, 2008.

Matrosov, S. Y., Mace, G. G., Marchand, R., Shupe, M. D., Hallar, A. G., and McCubbin, I. B.: Observations of ice crystal habits with a scanning polarimetric W-band radar at slant linear depolarization ratio mode, Journal of Atmospheric and Oceanic Technology, 29, 989–1008, https://doi.org/10.1175/JTECH-D-11-00131.1, 2012.

Matrosov, S. Y., Schmitt, C. G., Maahn, M., and de Boer, G.: Atmospheric Ice Particle Shape Estimates from Polarimetric Radar Measurements and In Situ Observations, Journal of Atmospheric and Oceanic Technology, 34, 2569–2587, https://doi.org/10.1175/JTECH-D-17-0111.1, 2017.

Middleton, D.: An Introduction to Statistical Communication Theory: An IEEE Press Classic Reissue, An IEEE Press classic reissue, Wiley, 1996.

Moisseev, D., von Lerber, A., and Tiira, J.: Quantifying the effect of riming on snowfall using ground-based observations, Journal of Geophysical Research (Atmospheres), 122, 4019–4037, https://doi.org/10.1002/2016JD026272, 2017.

Moisseev, D. N. and Chandrasekar, V.: Nonparametric Estimation of Raindrop Size Distributions from Dual-Polarization Radar Spectral Observations, Journal of Atmospheric and Oceanic Technology, 24, 1008, https://doi.org/10.1175/JTECH2024.1, 2007.

Morrison, H., van Lier-Walqui, M., Fridlind, A. M., Grabowski, W. W., Harrington, J. Y., Hoose, C., Korolev, A., Kumjian, M. R., Milbrandt, J. A., Pawlowska, H., Posselt, D. J., Prat, O. P., Reimel, K. J., Shima, S.-I., van Diedenhoven, B., and Xue, L.: Confronting the Challenge of Modeling Cloud and Precipitation Microphysics, Journal of Advances in Modeling Earth Systems, 12, e01689, https://doi.org/10.1029/2019MS001689, 2020.

Myagkov, A. and Unal, C.: W-band dataset with I/Q measurement for an AMT manuscript, https://doi.org/10.5281/zenodo.5126813, 2021.

Myagkov, A., Seifert, P., Wandinger, U., Bauer-Pfundstein, M., and Matrosov, S. Y.: Effects of antenna patterns on cloud radar polarimetric measurements, Journal of Atmospheric and Oceanic Technology, 32, 1813–1828, https://doi.org/10.1175/JTECH-D-15-0045.1, 2015.

Myagkov, A., Seifert, P., Bauer-Pfundstein, M., and Wandinger, U.: Cloud radar with hybrid mode towards estimation of shape and orientation of ice crystals, Atmospheric Measurement Techniques, 9, 469–489, https://doi.org/10.5194/amt-9-469-2016, 2016a.

Myagkov, A., Seifert, P., Wandinger, U., Bühl, J., and Engelmann, R.: Shape-temperature relationships of pristine ice crystals derived from polarimetric cloud radar observations during the ACCEPT campaign, Atmospheric Measurement Techniques Discussions, 2016, 1–37, https://doi.org/10.5194/amt-2015-365, 2016b.

Myagkov, A., Kneifel, S., and Rose, T.: Evaluation of the reflectivity calibration of W-band radars based on observations in rain, Atmospheric Measurement Techniques, 13, 5799–5825, https://doi.org/10.5194/amt-13-5799-2020, 2020.

Nadarajah, S. and Pogány, T. K.: On the distribution of the product of correlated normal random variables, 354, 201–204, https://doi.org/https://doi.org/10.1016/j.crma.2015.10.019, 2016.

Oue, M., Kumjian, M. R., Lu, Y., Verlinde, J., Aydin, K., and Clothiaux, E. E.: Linear depolarization ratios of columnar ice crystals in a deep precipitating system over the Arctic observed by zenith-pointing Ka-band Doppler radar, Journal of Applied Meteorology and Climatology, 54, 1060–1068, https://doi.org/10.1175/JAMC-D-15-0012.1, 2015.

Oue, M., Kollias, P., Ryzhkov, A., and Luke, E. P.: Toward Exploring the Synergy Between Cloud Radar Polarimetry and Doppler Spectral Analysis in Deep Cold Precipitating Systems in the Arctic, Journal of Geophysical Research (Atmospheres), 123, 2797–2815, https://doi.org/10.1002/2017JD027717, 2018.

Pfitzenmaier, L., Unal, C. M. H., Dufournet, Y., and Russchenberg, H. W. J.: Observing ice particle growth along fall streaks in mixed-phase clouds using spectral polarimetric radar data, Atmospheric Chemistry & Physics, 18, 7843–7862, https://doi.org/10.5194/acp-18-7843-2018, 2018.

Rodgers, C. D.: Inverse Methods for Atmospheric Sounding, WORLD SCIENTIFIC, https://doi.org/10.1142/3171, 2000.

Rusli, S. P., Donovan, D. P., and Russchenberg, H. W. J.: Simultaneous and synergistic profiling of cloud and drizzle properties using ground-based observations, Atmospheric Measurement Techniques, 10, 4777–4803, https://doi.org/10.5194/amt-10-4777-2017, 2017.

Ryzhkov, A. V., Snyder, J., Carlin, J. T., Khain, A., and Pinsky, M.: What Polarimetric Weather Radars Offer to Cloud Modelers: Forward Radar Operators and Microphysical/Thermodynamic Retrievals, Atmosphere, 11, 362, https://doi.org/10.3390/atmos11040362, 2020.

Skolnik, M.: Radar Handbook, McGraw-Hill Education, 3rd edn., 2008.

Spek, A. L. J., Unal, C. M. H., Moisseev, D. N., Russchenberg, H. W. J., Chandrasekar, V., and Dufournet, Y.: A new technique to categorize and retrieve the microphysical properties of ice particles above the melting layer using radar dual-polarization spectral analysis, Journal of Atmospheric and Oceanic Technology, 25, 482–497, https://doi.org/10.1175/2007JTECHA944.1, 2008.

Tridon, F. and Battaglia, A.: Dual-frequency radar Doppler spectral retrieval of rain drop size distributions and entangled dynamics variables, Journal of Geophysical Research (Atmospheres), 120, 5585–5601, https://doi.org/10.1002/2014JD023023, 2015.

Tridon, F., Battaglia, A., Luke, E., and Kollias, P.: Rain retrieval from dual-frequency radar Doppler spectra: validation and potential for a mid-latitude precipitating case-study, Quarterly Journal of the Royal Meteorological Society, 143, 1364–1380, https://doi.org/10.1002/qj.3010, 2017.

Tridon, F., Battaglia, A., Chase, R. J., Turk, F. J., Leinonen, J., Kneifel, S., Mroz, K., Finlon, J., Bansemer, A., Tanelli, S., Heymsfield, A. J., and Nesbitt, S. W.: The Microphysics of Stratiform Precipitation During OLYMPEX: Compatibility Between Triple-Frequency Radar and Airborne In Situ Observations, Journal of Geophysical Research (Atmospheres), 124, 8764–8792, https://doi.org/10.1029/2018JD029858, 2019.

Walpole, R. E., Myers, R. H., Myers, S. L., and Ye, K.: Probability and Statistics for Engineers and Scientists, Prentice Hall, 9th edn., 2012.

Wiener, N.: Generalized harmonic analysis, Acta mathematica, 55, 117–258, 1930.

Yoshikawa, E., Chandrasekar, V., and Ushio, T.: Raindrop Size Distribution (DSD) Retrieval for X-Band Dual-Polarization Radar, Journal of Atmospheric and Oceanic Technology, 31, 387–403, https://doi.org/10.1175/JTECH-D-12-00248.1, 2014.

Zhang, G., Mahale, V. N., Putnam, B. J., Qi, Y., Cao, Q., Byrd, A. D., Bukovcic, P., Zrnic, D. S., Gao, J., Xue, M., Jung, Y., Reeves, H. D., Heinselman, P. L., Ryzhkov, A., Palmer, R. D., Zhang, P., Weber, M., Mcfarquhar, G. M., Moore, B., Zhang, Y., Zhang, J., Vivekanandan, J., Al-Rashid, Y., Ice, R. L., Berkowitz, D. S., Tong, C.-c., Fulton, C., and Doviak, R. J.: Current Status and Future Challenges of Weather Radar Polarimetry: Bridging the Gap between Radar Meteorology/Hydrology/Engineering and Numerical Weather Prediction, Advances in Atmospheric Sciences, 36, 571–588, https://doi.org/10.1007/s00376-019-8172-4, 2019.